

WALLABY Pre-Pilot Survey: The effects of angular momentum and environment on the H I gas and star formation properties of galaxies in the Eridanus supergroup

C. Murugesan,^{1,2,3*} V. A. Kilborn,^{1,3} B.-Q. For,^{5,3} O. I. Wong,^{2,5,3} J. Wang,⁴
 T. Westmeier,^{5,3} A. R. H. Stevens,^{5,3} K. Spekkens,⁶ P. Kamphuis,⁷ L. Staveley-Smith,^{5,3}
 K. Lee-Waddell,^{8,3} D. Kleiner,⁹ B. S. Koribalski,^{8,10,3} M. E. Cluver,¹ S.-H. Oh,¹¹
 J. Rhee,^{5,3} B. Catinella,^{5,3} T. N. Reynolds,^{5,3} H. Dénes,¹² A. Elagali¹³

¹Centre for Astrophysics and Supercomputing, Swinburne University of Technology, Hawthorn, Victoria 3122, Australia

²ATNF, CSIRO, Space and Astronomy, PO Box 1130, Bentley, WA 6102, Australia

³ARC Centre of Excellence for All Sky Astrophysics in 3 Dimensions (ASTRO 3D), Australia

⁴Kavli Institute for Astronomy and Astrophysics, Peking University, Beijing 100871, China

⁵International Centre for Radio Astronomy Research, The University of Western Australia, 35 Stirling Highway, Crawley, WA 6009, Australia

⁶Royal Military College of Canada, PO Box 17000, Station Forces, Kingston, Ontario, Canada K7K 7B4

⁷Ruhr-Universität Bochum, Faculty of Physics and Astronomy, Astronomical Institute, 44780 Bochum, Germany

⁸ATNF, CSIRO, Space and Astronomy, PO Box 76, Epping, NSW 1710, Australia

⁹INAF – Osservatorio Astronomico di Cagliari, Via della Scienza 5, 09047 Selargius, CA, Italy

¹⁰Western Sydney University, Locked Bag 1797, Penrith, NSW 2751, Australia

¹¹Department of Physics and Astronomy, Sejong University, 209 Neungdong-ro, Gwangjin-gu, Seoul 05006, Republic of Korea

¹²ASTRON - The Netherlands Institute for Radio Astronomy, NL-7991 PD Dwingeloo, The Netherlands

¹³Telethon Kids Institute, Perth Children’s Hospital, Perth, Australia

Accepted XXX. Received YYY; in original form ZZZ

ABSTRACT

We use high-resolution ASKAP observations of galaxies in the Eridanus supergroup to study their H I, angular momentum and star formation properties, as part of the WALLABY pre-pilot survey efforts. The Eridanus supergroup is composed of three sub-groups in the process of merging to form a cluster. The main focus of this study is the Eridanus (or NGC 1395) sub-group. The baryonic specific angular momentum – baryonic mass ($j_b - M_b$) relation for the Eridanus galaxies is observed to be an unbroken power law of the form $j_b \propto M_b^{0.57 \pm 0.05}$, with a scatter of $\sim 0.10 \pm 0.01$ dex, consistent with previous works. We examine the relation between the atomic gas fraction, f_{atm} , and the integrated atomic disc stability parameter q (the $f_{\text{atm}} - q$ relation), and find that the Eridanus galaxies deviate significantly from the relation owing to environmental processes such as tidal interactions and ram-pressure affecting their H I gas. We find that a majority of the Eridanus galaxies are H I deficient compared to normal star-forming galaxies in the field. We also find that the star formation among the Eridanus galaxies may be suppressed owing to their environment, thus hinting at significant levels of pre-processing within the Eridanus sub-group, even before the galaxies have entered a cluster-like environment.

Key words: galaxies: evolution– galaxies: fundamental parameters– galaxies: ISM– galaxies: kinematics and dynamics

1 INTRODUCTION

The neutral atomic hydrogen (H I) gas in galaxies is a fundamental constituent, as it forms the primary reservoir from which molecular gas and eventually stars are formed. The H I gas content in galaxies is

set by both intrinsic properties and processes such as mass, angular momentum (AM), star formation and feedback, and/or a number of environmentally driven processes including tidal interactions and ram-pressure stripping. Therefore, studying the H I properties in relation to other observable global properties of galaxies, and the various processes that affect the H I gas is critical to our understanding of how galaxies evolve. In addition, the H I gas in galaxies

* E-mail: chandrashekar.murugesan@csiro.au

is typically more extended than their stellar discs (Verheijen & Sancisi 2001), making high (spatial and spectral) resolution H I observations of galaxies extremely important, as this allows us to trace the rotation curves of galaxies out to large radii. High-resolution H I observations of galaxies therefore not only enable us to study the kinematics of galaxies, but also accurately measure their AM.

It is well established that the H I gas fraction ($M_{\text{H I}}/M_{\star}$) of late-type galaxies is correlated with their stellar mass (M_{\star}), which is a commonly used scaling relation in H I astronomy (Haynes & Giovanelli 1984; Chamaraux et al. 1986; Solanes et al. 1996; Dénes et al. 2014). In addition, the H I content in galaxies has been observed to correlate with a number of other observables such as stellar surface mass density, NUV - r colour and the R -band magnitude (Catinella et al. 2010, 2012, 2018; Dénes et al. 2014; Brown et al. 2015, 2017). By studying these scaling relations for large samples of galaxies, we are able to understand how the H I gas content in galaxies is associated with other global properties. Galaxies that deviate from the mean trend of the various scaling relations are interesting, as they present to us an opportunity to probe the underlying physics driving their H I gas properties.

Among the various intrinsic properties of galaxies, mass and AM are believed to play important roles in regulating their H I content (see for example Zasov & Rubtsova 1989; Huang et al. 2012; Dénes et al. 2014; Maddox et al. 2015). Obreschcow et al. (2016) [hereafter O16] showed that the atomic gas fraction, $f_{\text{atm}} = \frac{1.35M_{\text{H I}}}{M_{\text{b}}}$, of disc galaxies is correlated with their integrated disc stability parameter $q = \frac{j_{\text{b}}\sigma}{GM_{\text{b}}}$, in the following manner,

$$f_{\text{atm}} = \min \left\{ 1, 2.5q^{1.12} \right\}, \quad (1)$$

where $M_{\text{H I}}$ is the H I mass of the galaxy, M_{b} is the total baryonic mass, j_{b} is the baryonic specific angular momentum (sAM), σ is the velocity dispersion of the Warm Neutral Medium (WNM) and G is the universal gravitational constant. Galaxies with a lower q will promote star formation processes driven by gas fragmentation and collapse, while larger values of q imply a higher stability against such mechanisms. The q parameter in this sense can be thought of as a global analog to the local Toomre parameter Q (Toomre 1964). A large sample of late-type galaxies from isolated environments (where the influence of environmental processes are minimal) are observed to follow the $f_{\text{atm}} - q$ relation consistently (O16; Lutz et al. 2017; Murugesan et al. 2019, 2020).

However, as mentioned earlier, the H I gas in galaxies can be easily influenced by environmental processes, which is particularly true in high-density environments, where processes such as tidal interactions (Merritt 1983; Byrd & Valtonen 1990; Rots et al. 1990), ram-pressure (Gunn & Gott 1972; Vollmer et al. 2001; Cayatte et al. 1994; Chung et al. 2009), strangulation (Larson et al. 1980), harassment (Moore et al. 1996) and thermal evaporation (Cowie & Songaila 1977) are prevalent. Such environmental processes have been observed to lower the H I gas fractions in late-type galaxies residing in high-density environments (see for example Davies & Lewis 1973; Giovanelli & Haynes 1985; Solanes et al. 2001; Dénes et al. 2014).

The O16 model is an idealized analytic model for equilibrium discs, and does not account for evolutionary or environmental processes that may be affecting the H I gas in galaxies. In order to understand how environmental effects affect galaxies in this parameter space, both simulation and observational studies are required. Stevens et al. (2018) used semi-analytic models (SAMs) for the first time to study the $f_{\text{atm}} - q$ parameter space, and found that two main environmental mechanisms – mergers and ram-pressure stripping –

were responsible for breaking the link between f_{atm} and q . However, empirical studies are necessary to test and verify this connection. The $f_{\text{atm}} - q$ parameter space thus provides the opportunity to identify galaxies whose H I gas fractions or AM properties have been affected by environmental processes.

While several theoretical studies have investigated the role of sAM and environment on the atomic gas fraction of galaxies (Lagos et al. 2017; Stevens et al. 2018, 2019; Wang et al. 2018; Zoldan et al. 2018), only two recent empirical investigations have studied the behaviour of galaxies on the $f_{\text{atm}} - q$ relation as a function of the galaxies' local environments. The first work was conducted by Li et al. (2020), who examined the behaviour of late-type galaxies in the Virgo cluster, using the VIVA sample (Chung et al. 2009). They observed that Virgo galaxies are not only conventionally H I-deficient relative to field galaxies of the same type, but they are also systematically offset below the $f_{\text{atm}} - q$ relation, indicating that environmental processes have significantly affected their H I gas content. By comparing their results with simulated data from the EAGLE simulations (Schaye et al. 2015), they attribute the H I-deficiency in the Virgo cluster galaxies to be driven primarily by ram-pressure stripping. Under this scenario, as galaxies are entering the cluster potential, ram-pressure effects take over and the galaxies lose a large fraction of their H I gas, which results in the overall reduction of their f_{atm} . However, the j_{b} values of these galaxies are not severely affected, which implies that the q values remain fairly unchanged. The combined result then is that galaxies will systematically drop off the $f_{\text{atm}} - q$ relation, supporting the earlier predictions made by Stevens et al. (2018, 2019).

The second empirical work to study the effects of the environment on galaxies in the $f_{\text{atm}} - q$ parameter space was undertaken by Murugesan et al. (2020) [hereafter M20]. They used 114 late-type galaxies from the WHISP survey (Swaters et al. 2002), in low- and intermediate density environments, and find that galaxies that are currently interacting (or have recently interacted, thereby accreting H I gas from their smaller companions) showed enhanced f_{atm} values, lower q values, and increased star formation rates (SFR) for their stellar mass. Interactions and mergers can have a significant influence on the way galaxies evolve. Lagos et al. (2018) used hydrodynamical simulations to study the effects of mergers on the stellar sAM (j_{\star}) of galaxies, and found that mergers tend to reduce j_{\star} , with dry major mergers showing the largest effect. However, they find that wet mergers on the other hand may marginally increase (by $\sim 10\%$) j_{\star} . Clearly, the location of galaxies in the $f_{\text{atm}} - q$ parameter space is governed by both M_{b} and j_{b} . In order to properly understand the behaviour of galaxies in this parameter space, it is imperative to populate this parameter space with galaxies from various environments and at various stages of their evolution.

The Widefield ASKAP L-Band Legacy All-sky Blind Survey (WALLABY; Koribalski et al. 2020) which aims to deliver high-resolution H I images for over 5000 galaxies uniformly across various environments, will be unprecedented in terms of its scope for enabling us to understand the different processes affecting the H I content of galaxies. WALLABY uses the Australian SKA Pathfinder (ASKAP; Hotan et al. 2021) as its survey instrument (see Section 2.1 for more details). With such a large sample, we will be able to populate the $f_{\text{atm}} - q$ parameter space systematically for the first time with galaxies from different environments, thus giving us the opportunity to study the degree of influence of both AM and environmental processes on the gas evolution of galaxies. In light of this, we make use of the WALLABY pre-pilot ASKAP observations of the Eridanus supergroup (see also For et al. 2021; Wong et al. 2021), to

study the influence of both AM and the environment on the H I gas content of the galaxies.

1.1 The Eridanus supergroup

As part of the Southern Sky Redshift Survey (SSRS; da Costa et al. 1988), the Eridanus group of galaxies was found to be part of a filamentary structure that encompassed the Fornax cluster and the Dorado group. Willmer et al. (1989) classified the Eridanus group of galaxies as a cluster composed of three to four subgroups. On the other hand, Garcia et al. (1993) and Barton et al. (1996) identified only two optically classified sub-groups, centered on NGC 1407 and NGC 1332 respectively. Omar & Dwarakanath (2005a) conclude that the Eridanus group of galaxies is a loose group.

A detailed investigation of the Eridanus group of galaxies was later made by Brough et al. (2006), who define this to be a supergroup, where three sub-groups of galaxies – the Eridanus (or NGC 1395), NGC 1407 and NGC 1332 sub-groups, are in the process of merging to form a cluster. They find that the NGC 1407 sub-group is the most evolved among the three sub-groups, and is composed of a large fraction of early-type galaxies, while the NGC 1395 and NGC 1332 sub-groups are observed to contain larger fractions of late-type galaxies. For consistency, here after, we will refer to the NCG 1395 sub-group as the Eridanus sub-group, which is the main focus of this study.

The NGC 1407 and NGC 1332 sub-groups have been studied as part of the Group Evolution Multiwavelength Study (GEMS) by Osmond & Ponman (2004). Using ROSAT X-ray data, both Trinchieri et al. (2000) and Brough et al. (2006) showed that there is extended X-ray emission associated with the NGC 1407 intragroup gas, while the X-ray emission from the NGC 1332 sub-group is localised to the NGC 1332 galaxy itself. Omar & Dwarakanath (2005a) also find intragroup X-ray emission associated with the Eridanus sub-group.

In addition, as part of the southern GEMS project, Kilborn et al. (2009) examined the H I properties of the NGC 1407 and NGC 1332 sub-groups using the 64-m Parkes single-dish telescope, and found that the H I gas distribution in the two groups differ, in the sense that for the NGC 1407 group there is a lack of H I in the central region of the group, while the NGC 1332 group is observed to have significantly more gas in the central region. Using high-resolution GMRT observations of the H I gas for a sub-sample of Eridanus galaxies, Omar & Dwarakanath (2005b) find that the Eridanus galaxies are about 2–3 times more H I-deficient compared to galaxies of similar type in the field. They suggest that the H I deficiency in the Eridanus galaxies is driven by tidal interactions rather than ram-pressure, as they observe that the level of ram-pressure is about two orders of magnitude lower compared to that in typical clusters.

A number of previous works have shown that even in the group regime, fast gas-removing processes such as ram-pressure cannot be fully ruled out, and are likely playing an important role in affecting the H I gas properties of the galaxies (Chamaraux & Masnou 2004; Kilborn et al. 2005, 2009; Sengupta & Balasubramanyam 2006; Westmeier et al. 2011; Hess & Wilcots 2013; Dénes et al. 2016; Brown et al. 2017; Stevens & Brown 2017). These studies hint at a scenario where a significant amount of pre-processing may be prevalent in group-like environments. The Eridanus supergroup is therefore an interesting field, as it is a supergroup composed of multiple sub-groups, which will eventually merge to form a cluster (Brough et al. 2006). Studying the H I and other global properties of the Eridanus galaxies therefore provides us the unique opportunity

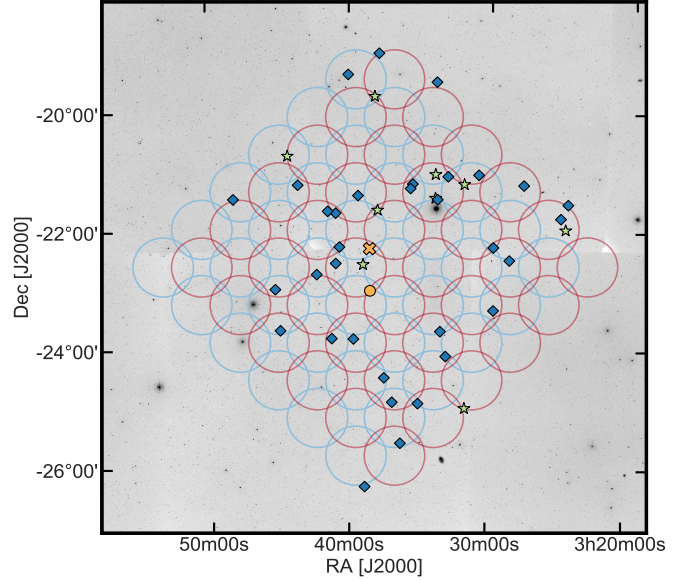


Figure 1. Footprints A (light blue) and B (red), overlaid on DSS image of the Eridanus field. The blue diamond points denote the Eridanus galaxies, while the background galaxies are represented by the green stars. The yellow circle represents the central large elliptical NGC 1395 of the Eridanus sub-group, while the yellow cross marks the centroid of the Eridanus sub-group derived by Brough et al. (2006), using a friends-of-friends group-finding algorithm.

to understand both the level of pre-processing within the different sub-groups as well as their in-fall boundaries.

2 DATA

2.1 Observations

The H I data for the current work has been acquired via ASKAP observations of the Eridanus supergroup, as part of the WALLABY pre-pilot survey efforts. ASKAP (Hotan et al. 2021) is a radio interferometer located at the Murchison Radio Observatory (MRO), in an isolated area in Western Australia. ASKAP consists of 36 antennas, each 12 m in diameter and equipped with the Mk II phased array feeds (PAFs; DeBoer et al. 2009; Chippendale et al. 2010; Hotan et al. 2014). Using the PAF technology, each ASKAP antenna is able to form 36 beams on the sky simultaneously. Typically, the 36 beams are arranged in a 6×6 square or diamond like pattern (also called footprints). Each footprint has a field of view (FOV) ~ 30 deg² at 1.4 GHz. By interleaving two footprints (footprint A and B), we achieve close to uniform rms across the field. The observations of the Eridanus field were carried out in March 2019, for both footprints A and B, with a combined integration time of 10.8 h. The observing strategy involved interleaving two diamond-shaped ASKAP footprints to mostly observe galaxies belonging to the Eridanus sub-group (see Fig. 1). The Eridanus sub-group is the first pre-pilot field for which observations were made with all 36 antennas and using a full bandwidth of 288 MHz. For a full description of the observations and quality of data, we refer the reader to For et al. (2021).

2.2 Data reduction

In this work, only 144 MHz of the data corresponding to the higher frequency end (1295.5 to 1439.5 MHz) of the total 288 MHz band was processed, as the Eridanus sub-group and the background galaxies are contained within this velocity range (1000 to 8100 km s⁻¹). The ASKAP observations have been reduced using the ASKAPSOFT pipeline [version 0.24.7] (Whiting 2020), which is the default software used to process and image ASKAP observations. The processing strategy involved first reducing the data for the two footprints independently, and then finally mosaicking the individual beams from each footprint to make the final image cubes. Standard processing steps were involved, such as flagging, bandpass calibration, continuum imaging, continuum subtraction, spectral imaging and image-based continuum subtraction. A Robust weighting of 0.5 was used for the spectral imaging step, and the final mosaicked cube was convolved to a resolution of 30 arcsec, and having a channel width of ~ 4 km s⁻¹, corresponding to the original channel resolution of 18.5 kHz. For more details on each processing step, we refer the reader to previous early science papers (Kleiner et al. 2019; Reynolds et al. 2019; Lee-Waddell et al. 2019; Elagali et al. 2019; For et al. 2019), which have described both ASKAPSOFT and the ASKAP pipeline in great length. The rms noise in the final mosaicked image cube is ~ 2.6 mJy per beam per channel, corresponding to a 3σ H I column density of $N_{\text{HI}} \sim 4 \times 10^{19} \text{ cm}^{-2}$. Following the image processing, SoFiA (Serra et al. 2015), an efficient source finding software was run on the final spectral cube to automatically detect the H I sources.

From the final mosaicked image cube, we split out smaller ($0.2 \times 0.2 \text{ deg}^2$) cubelets for the individual galaxy detections. However, as the signal-to-noise ratio (SNR) for many sources in the sample was low, we performed a Hanning smoothing along the velocity axis and smoothed the cubes to a 12 km s⁻¹ velocity resolution, in order to improve the SNR. This reduces the rms in the smoothed cubes to ~ 1.8 mJy per beam per channel, resulting in a 3σ H I column density limit of $N_{\text{HI}} \sim 8 \times 10^{19} \text{ cm}^{-2}$. We use these cubelets and the resulting moment-0 (intensity) and moment-1 (velocity) maps for the rest of the analysis in this work. For the full catalogue and description of the source properties, we refer the reader to For et al. (2021).

2.3 The sample

The final source catalogue from SoFiA consists of 55 H I detections – 43 detections in the Eridanus field and 12 detections corresponding to background field galaxies. Of the total 55 galaxies, we select galaxies that have an H I diameter, $D_{\text{HI, max}} \geq 120 \text{ arcsec}$, so that we have at least four resolution elements across the major axis, to be able to model the galaxies accurately using 3D fitting techniques (for more details see Section 2.4). $D_{\text{HI, max}}$ is the maximal H I diameter out to which the tilted-ring modelling is performed, and corresponds to the radius where the H I column density drops to the 3σ H I column density limit of $N_{\text{HI}} \sim 8 \times 10^{19} \text{ cm}^{-2}$. This is to ensure that we do not miss emission in the very outskirts of the galaxies, which also enables us to derive more accurate AM values. This selection criteria leaves us with the fiducial sample consisting of a total of 42 galaxies – 33 Eridanus galaxies and 9 background galaxies. The sample and all the relevant derived properties of the galaxies are listed in Table D1.

2.4 Measuring the total baryonic mass (M_b) and baryonic specific angular momentum (j_b)

We now describe the methods employed in this work to measure the total baryonic mass (M_b) and baryonic specific AM (j_b) for the sample galaxies. We first perform 3D tilted-ring fitting (Rogstad et al. 1974) using 3DBarolo (Di Teodoro & Fraternali 2015) for 42 of the 55 H I detections in the field. The remaining 13 detections were not well resolved for robust kinematic modelling, and for this reason they were omitted from the analysis. For a step-by-step description of the 3D fitting method, we refer the reader to Murugesan et al. (2019). The 3D modelling involves fitting n independent tilted rings (where n is the total number of resolution elements across the major axis) of width 15 arcsec (half the FWHM of the resolution element). In the fitting procedure we fix the kinematic centre to the optical/NIR centre (obtained from NED¹), and the systemic velocity and position angle (PA) to the values determined by SoFiA. For the inclination angle (i), we use the B -band optical surface photometry based estimate by Lauberts & Valentijn (1989), as the initial guess. We allow PA, i and the rotation velocity (v_{rot}) to vary as free parameters.

The fitting is performed in two stages – in the first stage the user-defined initial guesses for the galaxy centre, systemic velocity, PA, i and v_{rot} are assumed for the fitting, and in the second stage the code uses the best fit values from the first stage to fit the final model. We allow both the PA and i to vary within a range of $\pm 10^\circ$ about the inputted value for the fitting, thus enabling the code to reasonably model any kinematic warps. Once the best fitting model is derived, the code outputs the best fitting values for PA, i and v_{rot} for every ring. In order to verify the goodness of the fit, we inspect if the derived line-of-sight velocities $v_{\text{LOS}} = v_{\text{rot}} \sin(i)$ are in agreement with the position–velocity (PV) diagrams of the galaxies. In Appendix A, we present the fitted model parameters and PV diagrams for two specific galaxies to demonstrate the robustness of the modelling. The tilted-rings are then projected onto the moment-0 H I integrated flux map to compute the H I mass within each ring, using the following relation,

$$M_{\text{HI}} [M_\odot] = 2.356 \times 10^5 D^2 S_{\text{int}}, \quad (2)$$

where, D is the distance to the source in Mpc and S_{int} is the total integrated flux from all pixels enclosed within the ring in Jy km s⁻¹. We compute the uncertainties on M_{HI} by propagating the errors associated with D and S_{int} . We assume a nominal error of 10% on the distance (D) and compute the error on S_{int} using the relation introduced in Koribalski et al. (2004).

The stellar mass within each ring is calculated by projecting the tilted-rings onto the 2MASS (Skrutskie et al. 2006) K_s -band background subtracted mosaic of the galaxies. The sum of the K_s magnitudes within each ring is converted to a stellar mass following the relation described by Eq.3 in Wen et al. (2013) as follows

$$\log_{10} \left(\frac{M_\star}{M_\odot} \right) = (-0.498 \pm 0.002) + (1.105 \pm 0.001) \times \log_{10} \left(\frac{v L_v (K_s)}{L_\odot} \right). \quad (3)$$

Where L_v is the luminosity, derived using the extinction-corrected K_s -band magnitude.

The total H I and stellar masses are computed by summing their respective mass within each ring. The total baryonic mass is

¹ <http://ned.ipac.caltech.edu/>

calculated using the relation $M_b = M_\star + 1.35M_{\text{H I}}$, where $M_{\text{H I}}$ is the total H I mass and M_\star is the total stellar mass. The factor 1.35 accounts for the local universal 26% He fraction. The total baryonic specific AM is computed using the following relation

$$j_b = \frac{\sum_i (1.35M_{\text{H I},i} + M_{\star,i}) v_{\text{rot},i} r_i}{\sum_i (1.35M_{\text{H I},i} + M_{\star,i})} \quad (4)$$

Where, r_i is the radius of the i^{th} ring in kpc and $v_{\text{rot},i}$ is the rotation velocity corresponding to that ring in km s^{-1} .

We note the following approximations have been made in our analysis without significantly affecting our M_b and j_b measurements – a) As a large fraction ($\sim 76\%$) of the sample galaxies are low-mass spirals ($\log_{10}(M_\star)[M_\odot] < 9.5$) with no prominent bulge component, the potential contribution from the bulge to the M_b and j_b measurements will be negligible. We have therefore not implemented any corrections to account for this effect in our analysis. b) We have not accounted for the molecular gas (H_2) contribution in our measurements, as CO data are unavailable for the sample. However, the H_2 gas mass in low-mass spirals typically constitutes $\leq 6\%$ of the total baryonic mass (see for e.g., [Saintonge et al. 2017](#); [Isbell et al. 2018](#)). Therefore, the lack of H_2 data should not affect our M_b and j_b measurements by more than a few percent. c) Lastly, j_b is computed assuming that all baryonic matter (stars + H I gas) in the galaxies are co-moving with the same rotation velocity. This may not always be the case, however, the H I gas forms a dominant part of the total baryonic mass budget of the Eridanus galaxies, and is likely to be the largest contributor to their j_b values. We verify this by computing the ratio of the specific angular momentum of the H I gas to that of the stars, $j_{\text{H I}}/j_\star$, and plotting it against their total baryonic mass, M_b (Fig. B1 in Appendix B). We observe no correlation between $j_{\text{H I}}/j_\star$ and M_b and find that the mean value of $j_{\text{H I}}/j_\star \sim 2$ for the Eridanus sample (in agreement with the observations made by [Mancera Piña et al. \(2021a\)](#) for their sample of disc galaxies).

Finally, we compute the atomic gas fraction and stability parameter following [O16](#) as

$$f_{\text{atm}} = \frac{1.35M_{\text{H I}}}{M_b} \quad (5)$$

$$q = \frac{j_b \sigma_{\text{H I}}}{GM_b} \quad (6)$$

In this work, we have fixed the H I velocity dispersion ($\sigma_{\text{H I}}$) value to 10 km s^{-1} . This is mainly due to the following reasons – a) The H I cubes used for the 3D tilted-ring modelling were smoothed to a velocity resolution of 12 km s^{-1} (for details see Section 2.2), implying that fitting for $\sigma_{\text{H I}}$ which typically has values in the range $8 - 13 \text{ km s}^{-1}$ ([Leroy et al. 2008](#)) will no longer be reliable, making it hard to constrain the fitted $\sigma_{\text{H I}}$ value. b) As the SNR in the data cubes are low, having an additional free parameter to fit for will possibly make the overall fits less physically accurate. c) A number of previous works have shown that the mean $\sigma_{\text{H I}}$ value for large samples of late-type galaxies is $\sim 10 \text{ km s}^{-1}$ ([M20](#); [Mogotsi et al. 2016](#); [Tamburro et al. 2009](#)) and corresponds to the expected velocity dispersion driven by turbulence in the gas disc ([Tamburro et al. 2009](#); [Krumholz et al. 2018](#)).

The uncertainties on M_b , j_b , f_{atm} and q were calculated by propagating the errors associated with M_\star , $M_{\text{H I}}$ and v_{rot} using standard error propagation.

3 RESULTS

The majority of the detected galaxies in the Eridanus group are disc-dominated low-mass spirals and dwarfs (with a median stellar mass of $\log_{10}(M_\star)[M_\odot] \sim 8.8$). The fact that the Eridanus galaxies are low-mass systems and residing in high-density environments presents us with the opportunity to study the effects of environmental processes on their H I and star formation properties. In the following sections, we investigate the effects of mass and sAM, as well as the environment on the global properties of the Eridanus galaxies.

3.1 The $j_b - M_b$ relation

Fig. 2 shows the $j_b - M_b$ relation for 235 galaxies (including the Eridanus and background galaxies from the current work), gathered from studies which have accurately measured their j_b and M_b values. The sample includes 16 THINGS galaxies ([Walter et al. 2008](#)), for which the j_b and M_b measurements were made by ([Obreschcow & Glazebrook 2014](#)) [hereafter OG14], 14 dwarf galaxies from the LITTLE THINGS survey ([Hunter et al. 2012](#)) for which the measurements were made by [Butler et al. \(2017\)](#), 11 void dwarf galaxies from [Kurapati et al. \(2018\)](#), 38 late-type galaxies from the Virgo cluster from [Li et al. \(2020\)](#), 114 late-type galaxies from the WHISP sample ([Swaters et al. 2002](#)), for which the measurements were made by M20, 33 galaxies in the Eridanus supergroup and 9 background galaxies, both from this study. Collectively, this forms the largest sample of late-type galaxies to be studied on the $j_b - M_b$ parameter space. We fit² a linear regression to the relation (accounting for the errors on j_b and M_b) for all galaxies (excluding the Eridanus sample) and find a best fitting line with slope 0.55 ± 0.02 and intercept -2.65 ± 0.17 (solid black line in Fig. 2) with an intrinsic scatter of 0.16 dex. We also fit a line to the Eridanus galaxies alone and find a best fitting line with slope 0.57 ± 0.05 , intercept -3.06 ± 0.45 and an intrinsic scatter of 0.10 dex.

We perform an analysis of covariance (ANCOVA) hypothesis test to check if the slopes and intercepts of the $j_b - M_b$ relation for all galaxies and the Eridanus sample are statistically different. We find that the slopes of the two samples are not significantly different (p -value = 0.85) at an $\alpha = 0.05$ significance level. We then examined if the intercepts of the Eridanus sample and all other galaxies are statistically different and find that they are (p -value = 0). In Section 4 we discuss in more detail if this effect is simply due to selection biases associated with the different samples or driven by the environment.

3.2 The $f_{\text{atm}} - q$ relation for the Eridanus galaxies

Fig. 3 shows the distribution of the Eridanus galaxies (blue diamonds) in the $f_{\text{atm}} - q$ parameter space. We also plot the background galaxies (green stars) in order to compare their properties with the Eridanus sample. In addition, we also plot galaxies from relevant previous studies that have measured the f_{atm} and q values for galaxies residing in low-density environments (grey circles in Fig. 3). This includes the 16 late-type galaxies from the THINGS sample (O16), 14 dwarf galaxies from LITTLE THINGS ([Butler et al. 2017](#)), 13 H I-excess galaxies from the HIX survey ([Lutz et al. 2017](#)), 6 H I-deficient galaxies from [Murugesan et al. \(2019\)](#) and

² Fitting was performed using Hyper-Fit, an R package for fitting multi-dimensional data. See [Robotham & Obreschcow \(2015\)](#) for more details.

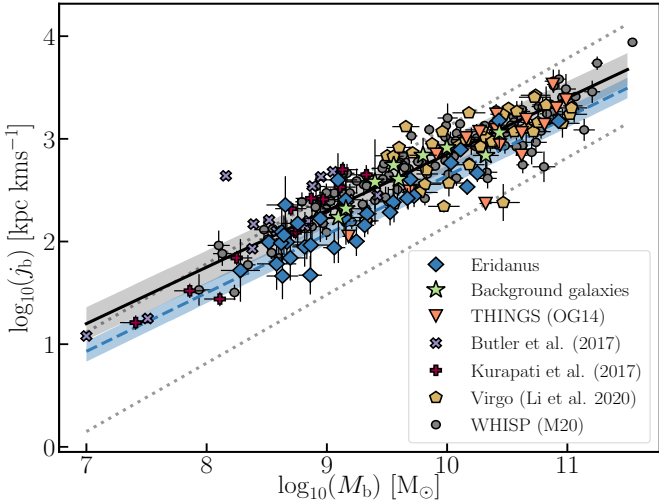


Figure 2. The $j_b - M_b$ relation for 235 late-type galaxies. The best fit line to all galaxies (solid black line) has a slope 0.55 ± 0.02 and 1σ scatter of 0.16 dex (light grey shaded region). The best fit line to the Eridanus galaxies alone (dashed blue line) has a slope 0.57 ± 0.05 and a scatter of 0.10 dex (light blue shaded region). The dotted lines show the expected range of j_b values based on Λ Cold Dark matter (Λ CDM) predictions (see OG14 for more details).

114 late-type galaxies from the WHISP sample from M20. The vast majority of the galaxies in this large sample follow the $f_{\text{atm}} - q$ relation consistently, including those that are conventionally categorised as H I-excess and H I-deficient. However, we find that most of the galaxies in the Eridanus sub-group deviate from the relation, where their observed f_{atm} values are significantly lower for their q values. This may be an indication that the Eridanus galaxies are subject to environmental effects such as tidal and ram-pressure stripping of the H I gas. A detailed discussion pertaining to the likely environmental processes that may be affecting the H I gas of galaxies in the Eridanus sub-group is made in Section 4.

In contrast, the background galaxies which are in the field behind the Eridanus supergroup are observed to follow the $f_{\text{atm}} - q$ relation consistently (see green stars in Fig. 3), as they are not likely to be affected severely by environmental processes. This result shows the stark contrast seen between the behaviour of galaxies residing in high- and low-density environments on the $f_{\text{atm}} - q$ parameter space.

The deviation of galaxies from the $f_{\text{atm}} - q$ relation driven by environmental effects can be used to quantify the level of H I deficiency in the galaxies (see Stevens et al. 2018, 2019; Li et al. 2020; Cortese et al. 2021). Galaxies that have significantly lower f_{atm} for their q are those systems whose H I gas has likely been stripped by environmental processes (e.g., Li et al. 2020). On the other hand, galaxies that have significantly higher f_{atm} values for their q are those systems that have possibly accreted gas from an interaction, and the H I gas has not yet settled into an equilibrium disc (see e.g., Wang et al. 2018; M20). In Section 3.4, we will use the $f_{\text{atm}} - q$ relation as a diagnostic plot to infer the H I deficiency among the Eridanus galaxies, by comparing their theoretically expected f_{atm} values with their observed f_{atm} values. This is a more physically motivated way to define H I deficiency driven by environmental processes, based on the disc stability of galaxies.

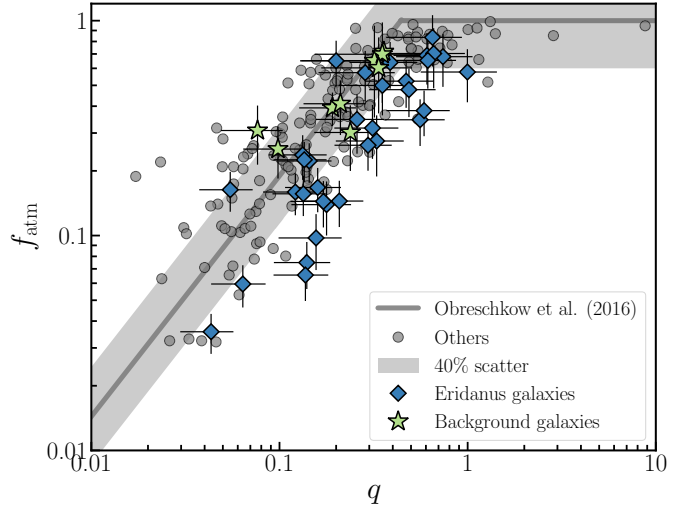


Figure 3. The relationship between the global disc stability parameter (q) and the atomic gas fraction (f_{atm}) of galaxies. Blue diamonds are the 33 Eridanus galaxies. The green stars are the background galaxies. The grey circles represent galaxies from previous studies exploring the $f_{\text{atm}} - q$ parameter space. The light grey region is defined in O16 as the 40% empirical intrinsic scatter in the H I velocity dispersion (σ_{HI}) of galaxies.

3.3 Effects of the local environment

In this section we present results and discuss the effects of the local environment on the f_{atm} and q values of the Eridanus galaxies. We probe the local density of the environment using the projected nearest-neighbour density metric (Σ_2 [Mpc^{-2}]), following the justifications made by M20. The Σ_2 metric is defined as $\Sigma_2 = 2/\pi D^2$, where D is the projected distance to the 2nd nearest-neighbour within $\pm 500 \text{ km s}^{-1}$. We compute the Σ_2 values using the 2MASS Redshift Survey (2MRS) catalogue (Huchra et al. 2012), which contains spectroscopic redshifts for over 43,500 galaxies with $K_s \leq 11.75$ mag and $|b| > 5^\circ$. The 2MRS survey is complete to 97.6% within these limits. As the 2MRS magnitude limits are based on K_s -band magnitudes, it is likely to be more sensitive to galaxies that are redder. To avoid any potential biases, we make the 2MRS catalogue volume-limited with the following two steps:

- (i) We first make a velocity cut to the original 2MRS catalogue, by selecting galaxies within the velocity range $200 - 12000 \text{ km s}^{-1}$.
- (ii) Following this, we add an absolute K_s -band magnitude cut to sources with $M_K < -23.45$, corresponding to the survey's limiting apparent magnitude of 11.75 mag at the highest velocity/redshift edge (12000 km s^{-1}). This makes the 2MRS sample volume-limited.

Fig. 4 shows the $f_{\text{atm}} - q$ relation for the Eridanus and background galaxies, with their Σ_2 values shown in the colour bar. Also plotted are the WHISP galaxies from M20, most of which are from relatively isolated environments or from loose groups. We see that the Σ_2 values for the Eridanus galaxies are significantly higher than those of the WHISP galaxies. Furthermore, we find that galaxies residing in higher densities show a larger deviation from the $f_{\text{atm}} - q$ relation compared to those in lower densities within the Eridanus supergroup. Additionally, in Section 3.4, where we explore the disc stability-based H I deficiency parameter, we show that galaxies residing in higher local densities are observed to have a larger H I-deficiency (see Fig. E1 in Appendix E). This result comes in support of the fact that galaxies with close neighbours in the

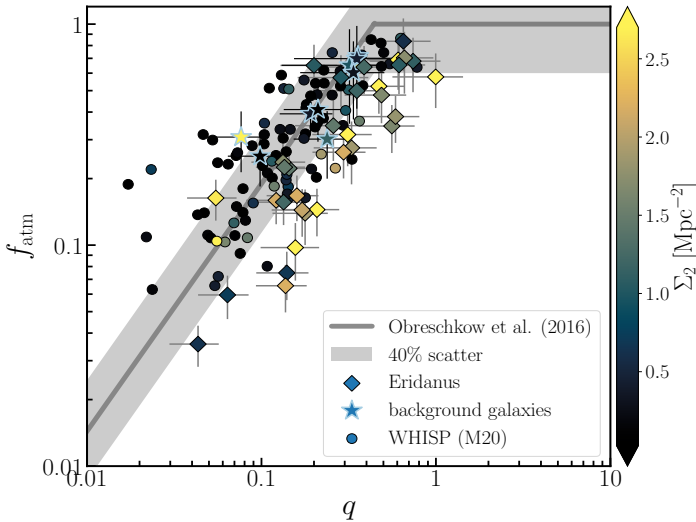


Figure 4. The $f_{\text{atm}} - q$ relation for the 33 Eridanus galaxies (diamonds), color-coded by their environment density, Σ_2 . For comparison, also plotted are WHISP galaxies (circles) from M20. We observe that the Eridanus galaxies are at comparatively higher environment densities compared to the WHISP galaxies. Also shown are the 9 background galaxies (stars), most of which are from low-density environments and follow the relation consistently.

Eridanus supergroup have possibly interacted previously and have lost a significant amount of their H I gas. In addition to the Eridanus galaxies, we also examine the behaviour of the background field galaxies in the $f_{\text{atm}} - q$ parameter space (indicated by the stars in Fig. 4). We see that all background galaxies (with the exception of one) are from relatively low-density environments compared to the Eridanus galaxies and follow the $f_{\text{atm}} - q$ relation consistently.

We also visually examined both the H I and optical morphology of the Eridanus galaxies in order to look for any signs of environmental effects. The H I gas is easily perturbed due to environmental processes such as tidal interactions and ram-pressure (Hibbard & van Gorkom 1996). Each of these processes leave different signatures on the H I and optical morphology of galaxies. Tidal interactions typically tend to affect both the H I gas and the stellar discs, where distortions and asymmetries in both the components can be observed (see for example Putman et al. 1998; Martinez-Delgado et al. 2010). Ram-pressure on the other hand usually only affects the H I gas, while the stellar component remains fairly unperturbed (Cayatte et al. 1994; Vollmer et al. 2001).

Upon examination, we find that most galaxies in the Eridanus sample show a disturbed H I morphology. Some galaxies are observed to have an asymmetric H I distribution without any sign of perturbation to their stellar discs, while others in the sample show both disturbed H I and stellar discs, hinting that a number of processes observed in high-density environments such as tidal interactions, minor mergers and ram-pressure effects may be prevalent in the Eridanus supergroup. This observation is consistent with a previous work that quantified the degree of lopsidedness of the H I gas among the Eridanus galaxies compared to field galaxies using Fourier component analysis of their H I maps (see Angiras et al. 2006). For a detailed discussion on the H I, optical and kinematic morphologies of individual galaxies in the Eridanus sample, we refer the reader to For et al. (2021). However, in the context of this work, we discuss the morphologies of a few select galaxies

that show signatures that are indicative of tidal and/or ram-pressure effects.

We first discuss candidates in our sample that show clear signs of ongoing tidal interactions, which is evidenced in their H I and optical morphology, as in the case of NGC 1359 and NGC 1385. NGC 1359 is in the process of a minor merger (Omar & Dwarakanath 2005a). The H I morphology of NGC 1359 is observed to be disturbed, with tidal plumes and tails associated with the galaxy. The optical image of the galaxy also shows a distorted and irregular stellar disc, indicative of an ongoing merger. NGC 1385 also shows signs of interaction. We observe an extended tidal tail to the south-west of the galaxy. The SFRs of both of these galaxies is significantly enhanced compared to the rest of the Eridanus galaxies. Tidal interactions and mergers among galaxies have been observed to enhance the SFR of the interacting galaxies (Kennicutt et al. 1987; Nikolic et al. 2004; Ellison et al. 2011). Additionally, such gas-rich interactions and minor mergers may lower the q values of the galaxies and increase their f_{atm} values (see Ellison et al. 2018; M20). We discuss this in more detail in Section 3.5 for these two galaxies, as a case study that demonstrates this behaviour.

A few galaxies in the Eridanus group show asymmetric H I morphologies (for example ESO482-G027, IC 1952, ESO482-G013) and/or exhibit truncated H I discs as in the case of NGC 1422, ESO548-G070 and IC 1953, without exhibiting any visible perturbations in their stellar discs. In Fig. 5 we show the H I contours of NGC 1422 and ESO482-G027 overlaid on top of their composite DSS optical images. It is clearly seen that NGC 1422 exhibits a truncated H I distribution compared to its stellar disc. ESO482-G027 is observed to have an extended tail-like feature towards the south-east end, with the H I contours compressed towards the north-west end, and the tail pointing away from the large group central galaxy NGC 1395.

This suggests that processes other than tidal interactions such as ram-pressure stripping may be prevalent in the Eridanus sub-group. In order to study the extent of influence of ram-pressure on the Eridanus galaxies, we compute the degree of ram-pressure exerted by the intra-group medium (IGM) of the Eridanus sub-group using the traditional formulation prescribed by Gunn & Gott (1972). The condition for ram-pressure stripping can be given as

$$\rho_{\text{IGM}} v_{\text{gal}}^2 \geq 2\pi G \Sigma_{\star} \Sigma_{\text{H I}}, \quad (7)$$

where ρ_{IGM} is the IGM density at the projected distance of the individual galaxies from the group central galaxy NGC 1395. v_{gal} is the relative velocity of the galaxies in the Eridanus sub-group with respect to the IGM, which can be approximated by the dispersion velocity of the Eridanus sub-group. Σ_{\star} and $\Sigma_{\text{H I}}$ denote the stellar and gas surface densities respectively, and G is the gravitational constant. As mentioned previously, diffuse X-ray emission surrounding NGC 1395 has been observed by previous studies (Trinchieri et al. 1986; Omar & Dwarakanath 2005b; Fukazawa et al. 2004). Fukazawa et al. (2004) make use of the archival ASCA X-ray data to model the diffuse X-ray surrounding the large central elliptical NGC 1395 in the Eridanus sub-group. They fit a single- β model by assuming a Raymond-Smith plasma (Raymond & Smith 1977) corresponding to an energy of ~ 0.76 keV and a solar abundance of 0.25. We use the following relation to estimate the IGM density at the projected distance to each galaxy in the Eridanus sub-group,

$$\rho_{\text{IGM}}(r) = \rho_{\text{IGM},0} \left[1 + \left(\frac{r}{r_c} \right)^2 \right]^{-3\beta/2}, \quad (8)$$

here, $\rho_{\text{IGM},0} = 10.2 \times 10^{-3} \text{ cm}^{-3}$ is the central IGM density, $r_c =$

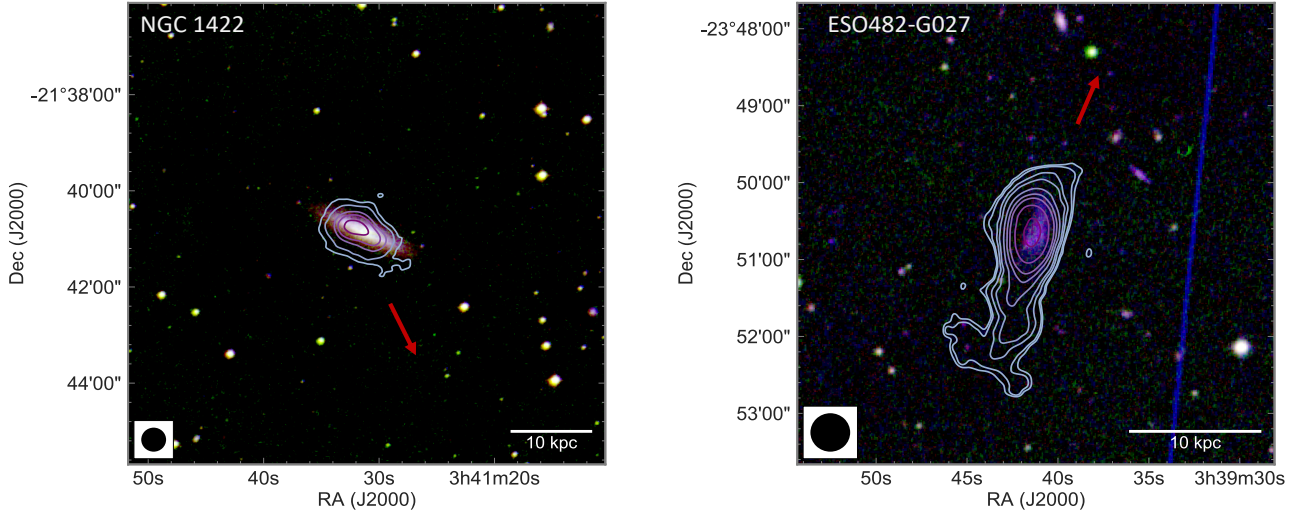


Figure 5. Two galaxies – NGC 1422 and ESO482-G027 – in the Eridanus sub-group exhibiting a truncated and lopsided H I distribution, respectively. The H I contours of the galaxies have been overlaid on top of their composite DSS optical images. The red arrows point in the direction of the large group central elliptical galaxy NGC 1395. In the case of NGC 1422, we find that the stellar disc does not show any signs of perturbation, while the H I gas distribution is severely truncated. This is a typical signature of galaxies affected by ram-pressure. ESO482-G027 on the other hand is observed to have an extended tail pointing away from the group central galaxy NGC 1395. In addition, we see that the H I contours are compressed to the north-west side of the galaxy. Both these features allude to ram-pressure effects. The contours for NGC 1422 correspond to column densities of 0.7, 2, 5, 7 and $10 \times 10^{20} \text{ cm}^{-2}$. The contours levels for ESO482-G027 are at 0.7, 0.9, 1.5, 2, 3, 4, 5, 7 and $10 \times 10^{20} \text{ cm}^{-2}$. For detailed maps of all the Eridanus and background galaxies, we refer the reader to the main catalogue paper by [For et al. \(2021\)](#)

3.7 kpc is the core radius and $\beta = 0.38$ is the exponent from the single- β model fit to the X-ray data by [Fukazawa et al. \(2004\)](#). The dispersion velocity of the Eridanus sub-group differs significantly between previous works. [Brough et al. \(2006\)](#) use a friends-of-friends algorithm and estimate the value to be $\sim 156 \text{ km s}^{-1}$, while [Tully \(2015\)](#) find the group velocity to be $\sim 228 \text{ km s}^{-1}$. We use both these values to approximate our uncertainty on the level of ram-pressure experienced by galaxies in the Eridanus sub-group. We find that assuming $v_{\text{gal}} = 156 \text{ km s}^{-1}$ for the group, only 7 of the 27 galaxies in the Eridanus sub-group may be affected by ram-pressure. However, when assuming $v_{\text{gal}} = 228 \text{ km s}^{-1}$, we find that as many as 13 galaxies ($\sim 48\%$) may be affected by ram-pressure to column densities $N_{\text{H I}} \leq 1.8 \times 10^{20} \text{ cm}^{-2}$. This may explain the curious case of some galaxies in the Eridanus supergroup exhibiting asymmetric H I morphologies and truncated H I discs (see Fig. 5).

3.4 H I deficiency in the Eridanus galaxies based on their disc stability

In the previous sections, we showed that the Eridanus galaxies deviate from the $f_{\text{atm}}-q$ relation, with galaxies having consistently lower f_{atm} values for their q values. We attribute this to environmental effects on the H I content of the Eridanus galaxies. In order to quantify the degree of this offset, we make use of the disc stability-based H I deficiency parameter (Δf_q) which was first briefly explored by [Stevens et al. \(2018\)](#), and later tested with empirical data by [Li et al. \(2020\)](#). Δf_q can be defined as follows (Eq. 4 in [Li et al. \(2020\)](#)),

$$\Delta f_q = \log_{10} \left(\min \left\{ 1, 2.5q^{1.12} \right\} \right) - \log_{10} (f_{\text{atm}}). \quad (9)$$

The more deficient in H I a galaxy is, the higher the value of Δf_q . According to the model in [O16](#), the atomic gas fraction (f_{atm}) in rotationally supported exponential disc galaxies depends on their q values. Unperturbed late-type galaxies will follow the relation con-

sistently as shown by previous studies ([Lutz et al. 2017](#); [Murugesan et al. 2019](#)), however, galaxies that are perturbed by environmental processes will deviate from the $f_{\text{atm}}-q$ relation ([Stevens et al. 2018](#); [Li et al. 2020](#); [M20](#)). The Δf_q parameter simply measures the difference in the expected f_{atm} value (for a given q) and the observed f_{atm} value of the galaxies.

Fig. 6 shows the distribution of the Δf_q values for the Eridanus and background galaxies. In addition, we also plot the WHISP galaxies from [M20](#), which are all late-type galaxies from low-density environments, for comparison. In this work, we define galaxies as H I-deficient if their $\Delta f_q > 0.2$ and H I-excess if their $\Delta f_q < -0.2$ (represented by the red vertical lines in Fig. 6). This is based on the observation that the intrinsic dispersion of galaxies following the $f_{\text{atm}}-q$ relation is ~ 0.2 dex for a large sample of normal star-forming late-type galaxies ([O16](#); [M20](#)).

The mean Δf_q value (with standard deviation included in brackets) for the Eridanus galaxies is found to be 0.31 (0.19). In comparison, the mean Δf_q value for the background and the WHISP galaxies is found to be -0.0025 (0.1476) and -0.011 (0.225). On the other extreme, we use the Δf_q values published by [Li et al. \(2020\)](#) for the Virgo cluster galaxies and find a mean Δf_q value of 0.57 (0.53), which is unsurprisingly higher than the Eridanus galaxies. Clearly, we see that the Eridanus galaxies are more H I deficient compared to galaxies from low-density environments, however they are not as deficient as galaxies in the Virgo cluster on average.

We perform several pairwise two-sample KS tests to examine if the distribution of the Δf_q values for the Eridanus, background and the Virgo galaxies are significantly different from the WHISP control sample. The KS test statistics are listed in Table. 1 for the different samples. We find that both the Eridanus and Virgo samples are significantly different (at a significance level of 5% or $\alpha = 0.05$) compared to the WHISP sample, while the background galaxies are not. This shows that the Eridanus galaxies are indeed significantly more H I-deficient compared to the normal star-forming galaxies in

Table 1. Two-sample KS test statistics for the different samples comparing their Δf_q distributions with that of the WHISP control sample. Δf_q values listed are the means for each sample, with the standard deviation given within brackets.

Sample	Size	Δf_q	D statistic	p -value
Eridanus	33	0.31 (0.19)	0.65	2.13×10^{-10}
Background	9	-0.0025 (0.1476)	0.25	0.6
Virgo	38	0.57 (0.53)	0.66	1.03×10^{-11}
WHISP	114	-0.011 (0.225)	-	-

the WHISP sample. Additionally, in Fig. E1 in Appendix E, we show that the Δf_q values of both the Eridanus and the WHISP galaxies are observed to increase with increasing local environment density (represented by Σ_2), consistent with a number of previous studies that have highlighted the effects of the dense environment on the H I gas fractions of galaxies (e.g. Giovanelli & Haynes 1985; Solanes et al. 2001; Dénes et al. 2014).

While traditional H I deficiency indicators are calibrated based on empirical samples of isolated late-type galaxies, the Δf_q parameter does not require any empirical sample for its calibration. It is purely based on the level of expected H I saturation in late-type disc galaxies for a given disc stability. It is therefore very straightforward to incorporate this parameter in both observational and simulation studies. In order to examine how the Δf_q parameter compares with more traditional H I deficiency parameters widely used in the literature, we plot the Δf_q values of the Eridanus galaxies against other H I deficiency indicators in Appendix C, and find a good positive correlation in general, albeit with large scatter.

In addition to its use as an H I-deficiency indicator, the Δf_q parameter has been shown to be useful in other ways. For instance, Stevens et al. (2018) in their semi-analytic study of the $f_{\text{atm}} - q$ parameter space introduced a parameter similar to Δf_q and used it to predict the absolute H I mass of galaxies that deviate from the $f_{\text{atm}} - q$ relation due to environmental effects (see Fig. 8 in their paper). Such predictions are very useful to design targeted H I surveys to detect galaxies that have a low H I gas fraction ($\log_{10}(M_{\text{HI}})[M_{\odot}] \leq 8$).

3.5 Star formation properties

In this section we present results pertaining to the star formation (SF) properties of the Eridanus and background galaxies, such as their specific star formation rate (sSFR = SFR/ M_{\star}) and H I based star formation efficiency (SFE = SFR/ M_{HI}), and compare them with the SF properties of a sample of late-type galaxies in low-density environments from the WHISP survey (M20). The objective of this analysis is to understand if and how the environment and internal properties such as mass and AM are playing a role in regulating the star formation in the sample galaxies.

We make use of both GALEX (Martin et al. 2005) and WISE (Wright et al. 2010) FUV and MIR photometries respectively, to estimate the SFR of the galaxies. The dust un-attenuated part of the total SFR is measured using GALEX FUV luminosities, while the dust attenuated part is measured using WISE W4 luminosities. For more details on the methods employed to measure the SFR for the Eridanus and background galaxies, we refer the reader to Wang et al. (2017) and For et al. (2021). We were able to derive robust SFR values for 26 of the 33 Eridanus galaxies and 5 of the 9 background galaxies. M20 were only able to measure the SFR for 86 of the 114 WHISP galaxies in their sample. The sample size for each of the

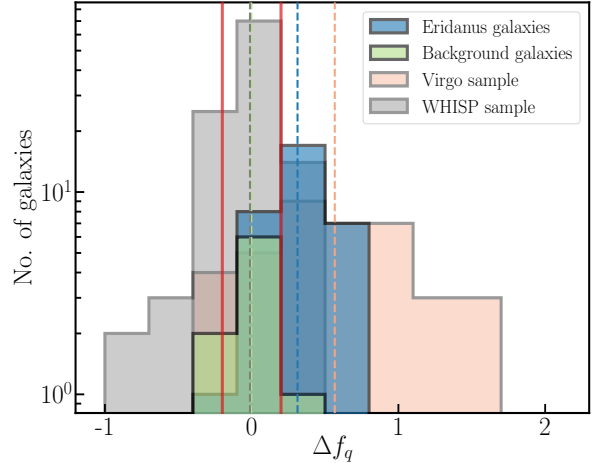


Figure 6. Distribution of the H I deficiency parameter, Δf_q , for the different samples. The red solid lines demarcate the H I-deficient, -normal and -excess regions and is equal to 0.2 dex. The blue, green, orange and grey dashed lines show the mean (with standard deviation included within brackets) Δf_q value for the Eridanus 0.31 (0.19), background -0.0025 (0.1476), WHISP -0.011 (0.225) from M20 and the Virgo samples 0.57 (0.53) from Li et al. (2020), respectively.

Table 2. KS test results for the Eridanus and background galaxy samples when comparing their sSFR distributions to the WHISP control sample (N=86).

Sample	Size	D statistic	p -value
Eridanus	26	0.38	0.0046
Background	5	0.41	0.3

three samples is therefore reduced to the above mentioned numbers for the rest of the analysis concerning their star formation properties.

Fig. 7a shows the distribution of the sSFR of the Eridanus, background and the WHISP galaxies. We find that the mean sSFR (with standard deviation in brackets) of the Eridanus galaxies is $\log_{10}(\text{sSFR}) [\text{yr}^{-1}] \approx -10.20(0.45)$, that for the background galaxies is $\log_{10}(\text{sSFR}) [\text{yr}^{-1}] \approx -9.69(0.34)$, while the mean sSFR of the WHISP sample is $\log_{10}(\text{sSFR}) [\text{yr}^{-1}] \approx -9.93(0.49)$. In addition, we also perform a two sample KS test to compare the sSFR distributions of the Eridanus and background galaxies with the WHISP control sample, and check if the two sample distributions are different from the control sample. Table. 2 shows the KS test results, and we find that the distribution of the sSFR values of the Eridanus galaxies differs significantly from the WHISP sample. In contrast, the background galaxies are not significantly different from the WHISP sample.

The sSFR value of the Eridanus galaxies on average being lower compared to both the WHISP and the background galaxies possibly hints at environmental effects influencing the star formation of the Eridanus galaxies. It has been observed that galaxies in low-density environments on average have higher sSFR compared to galaxies in high-density environments (see for example Moorman et al. 2016). Additionally, it has been shown that the sSFR of galaxies positively correlates with their H I gas fraction (Fumagalli & Gavazzi 2008; Zhou et al. 2018). As shown in the previous sections, the H I gas fraction (or f_{atm}) among the Eridanus galaxies is significantly lower for their q values. The H I deficiency is possibly

driven by environmental processes such as tidal interactions and ram-pressure. As such, we can associate the observed low sSFR among the Eridanus galaxies to environmental processes affecting their H I gas fractions. Within the Eridanus sample, we observe that the low-mass galaxies have a higher sSFR compared to the more massive (and low AM) systems. This is consistent with previous studies, and indicates that the star formation in low-mass systems contribute more to their growth compared to high-mass (and low AM) systems (see for example [Vulcani et al. 2010](#); [Zhou et al. 2018](#)), even in high-density environments such as the Eridanus sub-group.

[M20](#) found that galaxies that are currently interacting and actively accreting H I gas from their smaller dwarf companions showed enhanced SFR. In addition to this, they find that the f_{atm} values for such systems are higher, while their q values are reduced due to an overall reduction in j_b . In the Eridanus sample, NGC 1359 and NGC 1385 are currently undergoing a merger with their companions, and exhibiting clear signs in the form of tidal tails and debris, which are associated with the two galaxies. It is also observed that the sSFR of these two galaxies is enhanced, while the f_{atm} values are marginally higher than what is expected for their q (see Fig. 7b). These are the only two galaxies in the Eridanus sample that have $\Delta f_q < 0$, indicating that they are H I-normal (or even marginally H I-excess) for their integrated disc stability. The enhanced f_{atm} and sSFR may be associated with the accretion of fresh gas during the process of merging leading to increased star formation, consistent with the observations made by [Ellison et al. \(2018\)](#) and [M20](#).

In Fig. 8a, we show the distribution of the SFE of the Eridanus, background and WHISP galaxies. The mean (standard deviation within brackets) SFE of the Eridanus galaxies is found to be $\log_{10}(\text{SFE}) [\text{yr}^{-1}] \approx -9.76(0.41)$, while that of the background galaxies is $\log_{10}(\text{SFE}) [\text{yr}^{-1}] \approx -9.71(0.18)$. In comparison the mean SFE of the WHISP sample is found to be $\log_{10}(\text{SFE}) [\text{yr}^{-1}] \approx -9.54(0.60)$. It is interesting to note that the SFE of both the Eridanus and the background galaxies is comparable to the WHISP galaxies. This indicates that the SFE in galaxies may be regulated by the marginal disc stability model of late-type galaxies as postulated by [Wong et al. \(2016\)](#), where they find an average SFE of $\log_{10}(\text{SFE}) [\text{yr}^{-1}] \approx -9.65$ with a dispersion of 0.3 dex, for a large sample of galaxies (also see [Schiminovich et al. 2010](#); [Parkash et al. 2018](#)). We find that the observed SFE of both the Eridanus and the WHISP galaxies are consistent with this model. However, [Wong et al. \(2016\)](#) see a weak correlation between SFE and the surface brightness of gas and stars, which they attribute to the sAM of the galaxies.

In this work, we suggest that the SFE in late-type star-forming galaxies is mainly driven by the integrated disc stability parameter $q \propto j_b/M_b$, where both baryonic mass and AM have the ability to regulate the disc stability ([O16](#)). We see this effect in Fig. 8b for the different sample galaxies. We observe that galaxies with higher q values are found to have low SFE and correspondingly high f_{atm} values, and galaxies with low q values are found to have high SFE (and low f_{atm} values). This is due to the fact that galaxies with a higher disc stability prevent the collapse of H I gas to form molecular gas, and subsequently stars, and hence retain a high f_{atm} value as opposed to those galaxies with lower disc stability ([O16](#); [Stevens et al. 2018](#)). The fact that the Eridanus galaxies (which are from high-density environments) also follow this trend in the $f_{\text{atm}} - q$ parameter space, alludes to the point that mass and AM together play very important roles in determining the SFE of galaxies, via their ability to regulate the overall disc stability of late-type galaxies, irrespective of their environment.

Table 3. The star formation properties of the different samples. The sSFR and SFE values listed are the mean values for the different samples, with the standard deviation quoted within brackets.

Sample	Size	$\log_{10}(\text{sSFR})$ [yr^{-1}]	$\log_{10}(\text{SFE})$ [yr^{-1}]
Eridanus	26	-10.20(0.45)	-9.76(0.41)
Background	5	-9.69(0.34)	-9.71(0.18)
WHISP	86	-9.93(0.49)	-9.54(0.60)

4 DISCUSSION

We have shown that intrinsic properties such as mass and AM along with environmental processes play important roles in influencing both the H I gas and star formation properties of the Eridanus galaxies. In this section, we bring in some important discussion surrounding the observed results presented in Section 3, their interpretation, potential implications and associated caveats.

In Section 3.1 we presented the $j_b - M_b$ relation for the Eridanus galaxies and compared the distribution of the Eridanus galaxies with galaxies from other high-resolution H I surveys targeting late-type galaxies, including high- and low-mass spirals and dwarfs. It was observed that the slope of the $j_b - M_b$ relation for the Eridanus galaxies is statistically consistent with that of the larger sample of late-type galaxies. In addition, this slope is also consistent with the slope derived by previous works that have explored the $j - M$ space ([Romanowsky & Fall 2012](#); [Sweet et al. 2018](#); [Posti et al. 2018](#); [M20](#)). In a recent work, [Mancera Piña et al. \(2021b\)](#) examine the $j_b - M_b$ scaling relation for a sample of 157 galaxies ranging from dwarfs to high-mass spirals, and report a best fitting slope of 0.60 ± 0.02 with an intrinsic scatter 0.14 dex, consistent (within errors) with the fitted slopes in this work. The fact that independent studies using different samples and slightly different methods yield similar slopes is remarkable, and suggests that the $j_b - M_b$ relation indeed follows an unbroken power-law over five orders of magnitude in M_b . This has important implications for constraining our current cosmological models, and also serves as a great empirical benchmark for semi-analytic models to rely on.

While studying the $j_b - M_b$ relation for the Eridanus galaxies, we found that while the slope of the relation for the Eridanus galaxies and late-type galaxies from other surveys were statistically consistent, their intercepts were not. The j_b values for the Eridanus galaxies were on average lower (for the same M_b) compared to late-type galaxies from other surveys (see Fig. 2). It may be incorrect to associate the systematically lower j_b values of the Eridanus galaxies solely to environmentally driven processes. The observed discrepancy between the Eridanus sample and late-type and dwarf galaxies from other surveys may partly be arising due to selection biases. Most previous high-resolution H I surveys have selected their sample on the basis of the optical sizes and/or the stellar masses of the galaxies. They are often biased towards larger and more massive systems, implying that the selected galaxies are likely to be H I-normal or -excess, and thus likely to be high AM systems to start with. WALLABY on the other hand is a untargeted survey, meaning all galaxies within the detection limit of the survey are detected and hence is not particularly biased towards high AM systems. Thus, the systematically lower j_b of the Eridanus galaxies may be partly explained by arguing that galaxies from previous surveys are biased towards high j_b systems for the same M_b .

That being said, we cannot completely ignore the effects of environment on the j_b values of the Eridanus galaxies. [Fall \(1983\)](#) conducted the first empirical study that showed a tight correlation between the specific stellar specific AM (j_\star) and the stellar mass

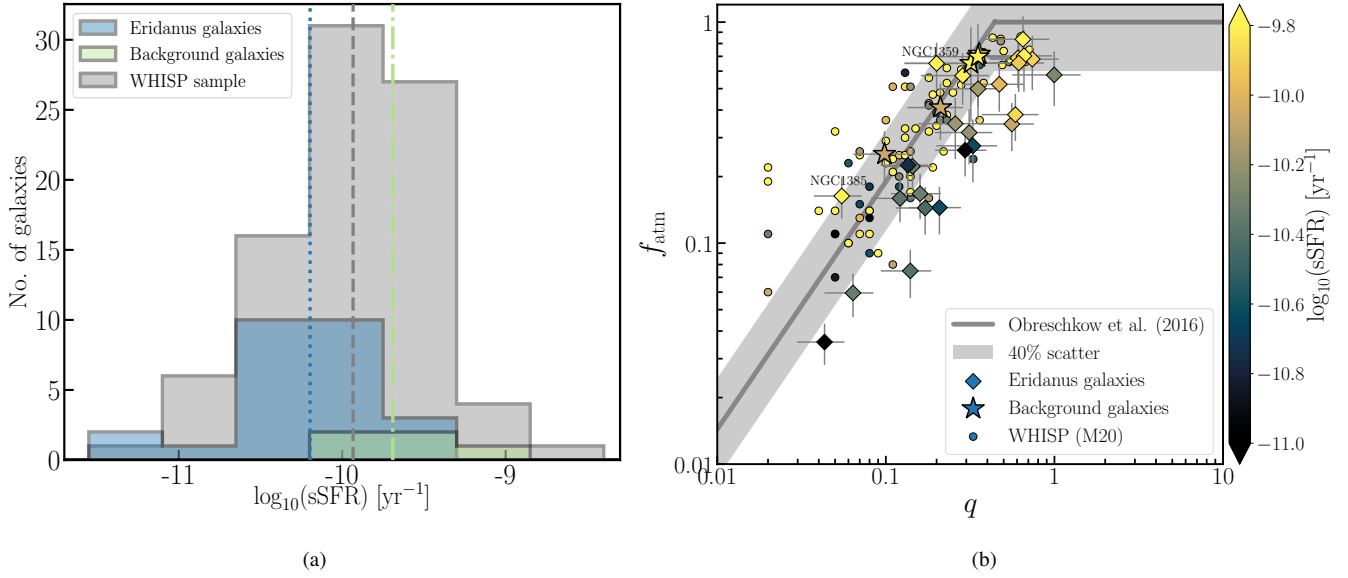


Figure 7. (a) Distribution of the sSFR of the Eridanus, background and WHISP samples. The mean value of the sSFR for the Eridanus, background and WHISP samples are represented by the blue dotted, green dash-dot and grey dashed lines respectively. (b) The $f_{\text{atm}} - q - \text{sSFR}$ parameter space for the 33 Eridanus galaxies (diamonds) and background galaxies (stars) color coded by their $\log_{10}(\text{sSFR})$ values. A general trend of increasing sSFR with increasing q is observed for the Eridanus galaxies. For comparison, also plotted are the 86 WHISP galaxies (circles) from M20. Also highlighted are two galaxies, NGC 1385 and NGC 1359 in the Eridanus sub-group, each of which are currently interacting with their companions. Such interacting systems have been observed to have higher f_{atm} values for their q , as they are actively accreting H I gas from their companions. This gas accretion results in the funneling of fresh gas to their centers to form stars hence enhancing their SFR (e.g. see Ellison et al. 2010; Ellison et al. 2018).

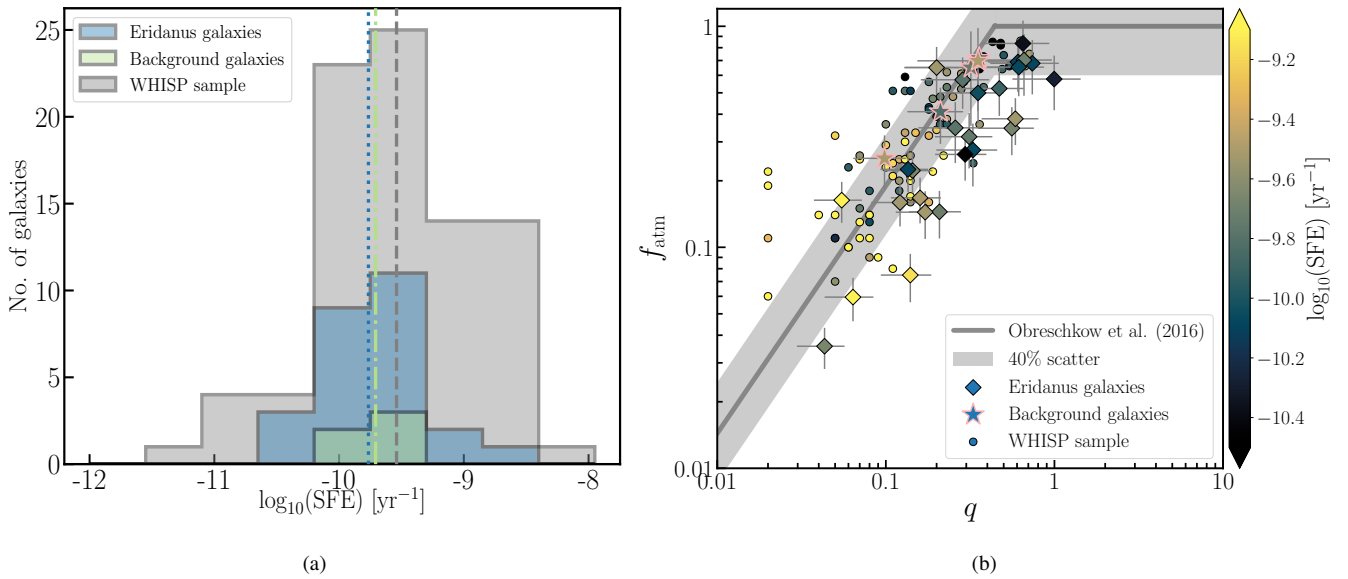


Figure 8. (a) Distribution of the SFE of the Eridanus, background and WHISP sample, with their mean values shown by the dotted blue, dash-dot green and dashed grey lines respectively. The distribution of the SFE of the three samples are consistent with each other and are observed to have a similar mean SFE (b) The $f_{\text{atm}} - q - \text{SFE}$ parameter space for the Eridanus (diamonds) and background galaxies (stars), color coded by their $\log_{10}(\text{SFE})$ values. Normal star-forming late-type galaxies from the WHISP sample (M20) are also shown (circles). A general trend of decreasing SFE with increasing q is observed, indicating that galaxies with a higher disc stability are inefficient in forming stars from their H I reservoir, consequently maintaining a higher H I gas fraction.

(M_{\star}) of galaxies. They found that both late- and early-type galaxies showed a linear correlation between $\log(j_{\star})$ and $\log(M_{\star})$, with a slope $\sim 2/3$. However, they observed that the j_{\star} values for early-type galaxies were over five times lower for a given M_{\star} compared to the late-type galaxies. In a follow-up work, Romanowsky & Fall (2012) confirmed this for a large sample of late- and early-type

galaxies. They link the observed lower j_{\star} values among early-type galaxies to interactions and mergers prevalent in higher density environments. Tidal interactions, in extreme cases, may lead to stripping of significant fractions of gas and stars in the galactic discs leading to a reduction in j_b (see Maller & Dekel 2002). In addition, tidal interactions between galaxies exert additional external torques on

the H I gas discs of the interacting galaxies, making the H I gas lose some of its AM and migrate to the centre of the galaxy (Barnes & Hernquist 1996) to form stars, which eventually contributes to the growth of a (pseudo) bulge (e.g. Courteau et al. 1996; Kormendy & Kennicutt 2004). Furthermore, hydrodynamic simulations have shown that dry mergers have the overall effect of reducing j_b (Lagos et al. 2018). It is therefore possible that the systematically lower j_b values observed among the Eridanus galaxies is also driven by environmental effects such as tidal interactions and galaxy harassment.

It is also worth noting that the j_b values of the majority of the Virgo cluster galaxies is in the expected range for their baryonic mass and morphological type (pentagons in Fig. 2). Li et al. (2020) argue that ram-pressure is the most dominant environmental process that is stripping the H I gas among the Virgo cluster galaxies. Ram-pressure typically removes the diffuse H I gas in the outskirts of galaxies first, which does not significantly affect the cumulative (or total) j_b and M_b values of the galaxies. As a result of this, the j_b , M_b and consequently the q values of galaxies undergoing ram-pressure stripping are not significantly affected.

It is well established that the cluster environment has an adverse effect on the H I gas fractions of galaxies, with a number of environmental processes affecting it (Davies & Lewis 1973; Giovanelli & Haynes 1985; Solanes et al. 2001). The effect of the group environment on the H I and AM properties of the constituent galaxies, however, is still not fully understood, and an area of active research. Over $\sim 50\%$ of galaxies reside in group-like environments (see for example Eke et al. 2004). Many studies have shown evidence of pre-processing in groups (Fujita 2004; Just et al. 2019), which affect the observed global properties of the constituent galaxies, such as their H I gas content (Cortese et al. 2006; Hess & Wilcots 2013; Džudžar et al. 2019a, 2019b), morphology, and star formation (Roberts & Parker 2017; Barsanti et al. 2018). This implies that galaxies in groups likely experience a significant level of pre-processing before such groups merge to form larger clusters. Since the Eridanus supergroup is composed of three sub-groups in the process of merging to form a cluster, it presents us with an opportunity to study the level of pre-processing among the galaxies in the sub-groups. While tidal interactions and mergers may be the dominant environmental processes affecting galaxies in the group regime, the effects of ram-pressure, specifically from groups that show signs of hot diffuse ionized gas in their IGM cannot be neglected (see for example Marcolini et al. 2003; Chamaroux & Masnou 2004; Sengupta & Balasubramanyam 2006; Mayer et al. 2006; Rasmussen et al. 2008; Dénes et al. 2016; Marasco et al. 2016; Brown et al. 2017).

Furthermore, in the context of the $f_{\text{atm}} - q$ framework, one cannot fully explain the behaviour of the Eridanus galaxies consistently falling below the $f_{\text{atm}} - q$ relation by only invoking tidal interactions as the gas removing mechanism. Semi-analytic simulations by Stevens et al. (2018) showed that ram-pressure and quasar driven winds from minor mergers are two important processes that can move galaxies below the $f_{\text{atm}} - q$ relation. Given these arguments, the effects of ram-pressure stripping and minor mergers are possibly needed in addition to tidal stripping to explain the observed deviation of the Eridanus galaxies below the $f_{\text{atm}} - q$ relation. As mentioned in Section 3.3, the H I maps of select galaxies in the Eridanus sample do indeed exhibit features observed in galaxies affected by ram-pressure, such as asymmetric and truncated H I discs, as well as compressed H I contours towards one side, which additionally come in support of the argument in favour of ram-pressure. In addition, the majority of the Eridanus galaxies are dwarfs or low-mass spirals (with a median stellar mass $\log_{10}(M_{\star})[M_{\odot}] \sim 8.8$),

making it easier for ram-pressure assisted by tidal interactions to strip off the H I gas. The behaviour of the Eridanus galaxies in the $f_{\text{atm}} - q$ parameter space is also consistent with a previous study of the Virgo cluster galaxies by Li et al. (2020), where ram-pressure effects have been observed to significantly reduce the f_{atm} values of the galaxies, thereby making them lie consistently below the $f_{\text{atm}} - q$ relation.

It should however be noted that the degree of influence of ram-pressure on the H I gas of galaxies is strongly dependent on their orbit, as well as their orientation (Vollmer et al. 2001; Jáchym et al. 2007; Stevens et al. 2019). The main caveat of the current analysis is that we do not have prior information regarding the orbits of the galaxies in the Eridanus sub-group, and have only used the projected distances of the galaxies from the central elliptical NGC 1395, to compute the level of ram-pressure experienced by the galaxies. The calculations also assume that the galaxies are moving face-on in the direction of motion. The current analysis is therefore only a first order approximation to probe the level of ram-pressure in the Eridanus sub-group. Contrary to our interpretations, Omar & Dwarkanath (2005b) argue that the H I deficiency among the Eridanus galaxies is mainly driven by tidal interactions. While this may be true, based on our observations, we conclude that other environmental processes are also likely playing a role in affecting the H I gas of the Eridanus galaxies.

5 CONCLUSIONS

We have used ASKAP H I observations of the Eridanus galaxies, to study their H I, angular momentum (AM) and star formation properties, as part of the WALLABY pre-pilot commissioning survey. We summarise the important findings of this work, and also discuss some future prospects.

- We have measured the total baryonic mass and total baryonic specific AM of the Eridanus and background galaxies, using robust rotation curves derived from 3D kinematic modelling of their H I gas distribution. We examined the $j_b - M_b$ relation for the Eridanus galaxies and find that the slope of the $j_b - M_b$ relation is 0.57 ± 0.05 , consistent with other studies that have probed the relation for late-type galaxies.
- We have explored the behaviour of the Eridanus and background galaxies in the $f_{\text{atm}} - q$ parameter space (see O16), and find that the Eridanus galaxies lie consistently off and below the $f_{\text{atm}} - q$ relation. This is suggestive that environmental processes such as tidal interactions and ram-pressure stripping are prevalent in the Eridanus sub-group, which have removed a significant fraction of the H I gas from the galaxies, making them H I deficient for their q values. In contrast, the background galaxies, which are from low-density environments follow the $f_{\text{atm}} - q$ relation consistently.
- Further, we examined the effects of the local environment on the Eridanus galaxies. We estimated the local density using the projected 2nd nearest-neighbour metric (Σ_2 [Mpc^{-2}]), and find that galaxies within the Eridanus sub-group with higher Σ_2 values are seen to deviate more from the $f_{\text{atm}} - q$ relation, again alluding to the fact that galaxies at higher local densities are influenced by their environment more than galaxies residing in lower densities. We also examined the H I and optical morphologies of the Eridanus galaxies and find that most galaxies in the Eridanus sample show a disturbed H I morphology. Some Eridanus galaxies exhibit asymmetric H I morphologies and truncated H I discs, but with no visible perturbations to their stellar component. These signatures are typical of ram-pressure effects. We computed the level of ram-pressure in the

Eridanus sub-group following the traditional method introduced by Gunn & Gott (1972) and find that over $\sim 48\%$ of the galaxies part of the Eridanus sub-group may have been influenced by ram-pressure. We thus conclude that both tidal interactions and ram-pressure are playing important roles in influencing the H I content of the Eridanus galaxies.

- We measure the H I deficiency among the Eridanus and the background galaxies in the context of their disc stability (q), by measuring the offset in their observed f_{atm} values with respect to the expected theoretical f_{atm} . We find that a majority of the Eridanus galaxies are significantly H I deficient for their integrated disc stability. We also compare the H I deficiency of the Eridanus galaxies with normal star-forming galaxies in low-density environments (M20), and find that the Eridanus galaxies are indeed H I deficient. In contrast, the background galaxies are found to be H I-normal.

- Finally, we examined the star formation properties of the sample galaxies by studying their sSFR and star formation efficiency (SFE), and their behaviour in the $f_{\text{atm}} - q$ parameter space. We find that star formation in the Eridanus galaxies may be marginally suppressed due to environmental effects. We find that the SFE of galaxies, irrespective of their environments, tend to decrease with increasing q . This is consistent within the original theoretical framework of O16, where galaxies with high q values are expected to have low SFE and vice versa, due the ability of q to regulate the collapse of H I gas to form molecular gas and eventually stars.

We have shown that pre-processing is prevalent in the Eridanus sub-group, which is in the processes of merging with at least two other sub-groups, and will eventually form a cluster (Brough et al. 2006). While tidal interactions among galaxies is believed to be the most common environmental process driving the H I deficiency in group environments, we have shown here that in the Eridanus sub-group, which hosts a hot IGM, there is evidence of ram-pressure (also causing a depletion of the galaxies' H I gas.

The $f_{\text{atm}} - q$ parameter space has shown great potential to probe the H I gas fractions of galaxies in the context of their mass and AM. It is proving to be a very useful parameter space, where trends in galaxies' SFR, sSFR, SFE and bulge-to-total ratio (a proxy for morphology) has been observed (M20), in addition to its ability to predict the expected H I saturation (or gas fraction) among rotationally dominated late-type galaxies. The $f_{\text{atm}} - q$ relation is being increasingly used as a diagnostic tool to identify various environmental effects on the H I gas of galaxies. For instance, Li et al. (2020) find that galaxies affected by ram-pressure, tend to consistently fall off the $f_{\text{atm}} - q$ relation, while M20 find that galaxies that are currently interacting and accreting H I gas tend to have higher f_{atm} for their q . This gives us a handle on the most dominant environmental process affecting the H I gas fractions in galaxies. Furthermore, the $f_{\text{atm}} - q$ parameter space provides us with a new physically motivated estimate of the H I deficiency (Δf_q) among late-type galaxies as demonstrated by Li et al. (2020), where Δf_q is simply the difference in the theoretically expected f_{atm} value (for a given q) and the observed f_{atm} of the galaxy. In this work, we have used this H I deficiency parameter to measure the extent of the H I deficiency among the Eridanus galaxies. We have additionally also compared the Δf_q H I deficiency parameter with more traditionally used H I deficiency parameters, and find a good one-to-one agreement, further validating the potential and robustness of this parameter.

While several simulation studies have explored the $j_b - M_b$ and $f_{\text{atm}} - q$ relations for statistically large samples of galaxies (e.g. Stevens et al. 2018; Lagos et al. 2018; Stevens et al. 2019),

empirical studies of the same are still limited to sample sizes of only a few hundred galaxies. WALLABY has the potential to resolve the gas structure of ~ 5000 galaxies in high resolution (Koribalski et al. 2020), thus positing the ability to accurately measure both the AM and H I properties for a large sample of galaxies. Using this wealth of data, we can then study the behaviour of galaxies across various environments on the $j_b - M_b$ and $f_{\text{atm}} - q$ parameter spaces. Such studies will be invaluable to our understanding of the degree of influence of internal parameters (such as mass and AM) and environmental factors, on the observed global properties of galaxies. We have demonstrated in this study that the reasonably high resolution (30 arcsec) H I observations, combined with a good velocity resolution (4 km s^{-1}) yield robust rotation curves, which is crucial for an accurate measurement of the AM in galaxies. In a future work, we aim to study the AM and H I properties of cluster galaxies, by observing their behaviour on the $f_{\text{atm}} - q$ relation. Since these galaxies are from extreme environments, do we expect to see galaxies deviating from the $f_{\text{atm}} - q$ relation as was observed by Li et al. (2020) among the Virgo cluster galaxies? How do cluster environments affect the AM, H I and star formation properties of galaxies? Such follow-up studies are important to test the full potential of this new parameter space. With the WALLABY survey anticipated to commence full operations in 2021, we hope to answer some of these questions, which will allow us to further our understanding of galaxy evolution across environments.

ACKNOWLEDGEMENTS

We thank the anonymous referee for their useful comments which considerably improved the quality of the paper. CM would like to thank Christopher Fluke, Robert Džudzar and Elaine Sadler for useful discussions and comments. CM is supported by the Swinburne University Postgraduate Award (SUPRA). ARHS acknowledges receipt of the Jim Buckee Fellowship at ICRAR-UWA. PK is partially supported by the BMBF project 05A17PC2 for D-MeerKAT. MEC is a recipient of an Australian Research Council Future Fellowship (project No. FT170100273) funded by the Australian Government. SHO acknowledges a support from the National Research Foundation of Korea (NRF) grant funded by the Korea government (Ministry of Science and ICT: MSIT) (No. NRF-2020R1A2C1008706).

This research was supported by the Australian Research Council Centre of Excellence for All Sky Astrophysics in 3 Dimensions (ASTRO 3D), through project number CE170100013.

The Australian SKA Pathfinder is part of the Australia Telescope National Facility which is managed by CSIRO. Operation of ASKAP is funded by the Australian Government with support from the National Collaborative Research Infrastructure Strategy. ASKAP uses the resources of the Pawsey Supercomputing Centre. Establishment of ASKAP, the Murchison Radio-astronomy Observatory and the Pawsey Supercomputing Centre are initiatives of the Australian Government, with support from the Government of Western Australia and the Science and Industry Endowment Fund. We acknowledge the Wajarri Yamatji people as the traditional owners of the Observatory site.

This publication makes use of data products from the Two Micron All Sky Survey, which is a joint project of the University of Massachusetts and the Infrared Processing and Analysis Center/California Institute of Technology, funded by the National Aeronautics and Space Administration and the National Science Foundation.

This research has made use of the NASA/IPAC Extragalactic

Database (NED), which is operated by the Jet Propulsion Laboratory, California Institute of Technology, under contract with the National Aeronautics and Space Administration.

This publication makes use of data products from the Wide-field Infrared Survey Explorer, which is a joint project of the University of California, Los Angeles, and the Jet Propulsion Laboratory/California Institute of Technology, funded by the National Aeronautics and Space Administration.

Parts of the results in this work make use of the colourmaps in the CMasher package (van der Velden 2020).

DATA AVAILABILITY

All data underlying this article is available within the article and enlisted in Table D1 in Appendix D. In addition, the calibrated visibility data and the processed image cubes of the Eridanus footprints are available to the public through the CSIRO ASKAP Science Data Archive (CASDA), via this DOI: <https://dx.doi.org/10.25919/0yc5-f769>

REFERENCES

- Angiras R. A., Jog C. J., Omar A., Dwarakanath K. S., 2006, *MNRAS*, **369**, 1849
- Barnes J. E., Hernquist L., 1996, *ApJ*, **471**, 115
- Barsanti S., et al., 2018, *ApJ*, **857**, 71
- Barton E., Geller M., Ramella M., Marzke R. O., da Costa L. N., 1996, *AJ*, **112**, 871
- Brough S., Forbes D. A., Kilborn V. A., Couch W., Colless M., 2006, *MNRAS*, **369**, 1351
- Brown T., Catinella B., Cortese L., Kilborn V., Haynes M. P., Giovanelli R., 2015, *MNRAS*, **452**, 2479
- Brown T., et al., 2017, *MNRAS*, **466**, 1275
- Butler K. M., Obreschkow D., Oh S.-H., 2017, *ApJL*, **834**, L4
- Byrd G., Valtonen M., 1990, *ApJ*, **350**, 89
- Catinella B., et al., 2010, *MNRAS*, **403**, 683
- Catinella B., et al., 2012, *A&A*, **544**, A65
- Catinella B., et al., 2018, *MNRAS*, **476**, 875
- Cayatte V., Kotanyi C., Balkowski C., van Gorkom J. H., 1994, *AJ*, **107**, 1003
- Chamaraux P., Masnou J.-L., 2004, *MNRAS*, **347**, 541
- Chamaraux P., Balkowski C., Fontanelli P., 1986, *A&A*, **165**, 15
- Chippendale A. P., O’Sullivan J., Reynolds J., Gough R., Hayman D., Hay S., 2010, in *Phased Array Systems and Technology (ARRAY)*, pp 648–652, doi:10.1109/ARRAY.2010.5613298
- Chung A., van Gorkom J. H., Kenney J. D. P., Crowl H., Vollmer B., 2009, *AJ*, **138**, 1741
- Cortese L., Gavazzi G., Boselli A., Franzetti P., Kennicutt R. C., O’Neil K., Sakai S., 2006, *A&A*, **453**, 847
- Cortese L., Catinella B., Smith R., 2021, arXiv e-prints, p. arXiv:2104.02193
- Courteau S., de Jong R. S., Broeils A. H., 1996, *ApJL*, **457**, L73
- Cowie L. L., Songaila A., 1977, *Nature*, **266**, 501
- Davies R. D., Lewis B. M., 1973, *MNRAS*, **165**, 231
- DeBoer D. R., et al., 2009, *Proceedings of the IEEE*, **97**, 1507
- Dénes H., Kilborn V. A., Koribalski B. S., 2014, *MNRAS*, **444**, 667
- Dénes H., Kilborn V. A., Koribalski B. S., Wong O. I., 2016, *MNRAS*, **455**, 1294
- Di Teodoro E. M., Fraternali F., 2015, *MNRAS*, **451**, 3021
- Džudžar R., et al., 2019a, *MNRAS*, **483**, 5409
- Džudžar R., Kilborn V., Murugesan C., Meurer G., Sweet S. M., Putman M., 2019b, *MNRAS*, **490**, L6
- Eke V. R., et al., 2004, *MNRAS*, **355**, 769
- Elagali A., et al., 2019, *MNRAS*, **487**, 2797
- Ellison S. L., Patton D. R., Simard L., McConnachie A. W., Baldry I. K., Mendel J. T., 2010, *MNRAS*, **407**, 1514
- Ellison S. L., Nair P., Patton D. R., Scudder J. M., Mendel J. T., Simard L., 2011, *MNRAS*, **416**, 2182
- Ellison S. L., Catinella B., Cortese L., 2018, *MNRAS*, **478**, 3447
- Fall S. M., 1983, in Athanassoula E., ed., *IAU Symposium Vol. 100, Internal Kinematics and Dynamics of Galaxies*, pp 391–398
- For B. Q., et al., 2019, *MNRAS*, **489**, 5723
- For B.-Q., et al., 2021, *MNRAS*
- Fujita Y., 2004, *PASJ*, **56**, 29
- Fukazawa Y., Makishima K., Ohashi T., 2004, *PASJ*, **56**, 965
- Fumagalli M., Gavazzi G., 2008, *A&A*, **490**, 571
- Garcia A. M., Paturel G., Bottinelli L., Gouguenheim L., 1993, *A&AS*, **98**, 7
- Giovanelli R., Haynes M. P., 1985, *ApJ*, **292**, 404
- Gunn J. E., Gott III J. R., 1972, *ApJ*, **176**, 1
- Haynes M. P., Giovanelli R., 1984, *AJ*, **89**, 758
- Hess K. M., Wilcots E. M., 2013, *AJ*, **146**, 124
- Hibbard J. E., van Gorkom J. H., 1996, *AJ*, **111**, 655
- Hotan A. W., et al., 2014, *Publications of the Astronomical Society of Australia*, **31**, e041
- Hotan A. W., et al., 2021, *Publ. Astron. Soc. Australia*, **38**, e009
- Huang S., Haynes M. P., Giovanelli R., Brinchmann J., 2012, *ApJ*, **756**, 113
- Huchra J. P., et al., 2012, *ApJSS*, **199**, 26
- Hunter D. A., et al., 2012, *AJ*, **144**, 134
- Isbell J. W., Xue R., Fu H., 2018, *ApJL*, **869**, L37
- Jáchym P., Palouš J., Köppen J., Combes F., 2007, *A&A*, **472**, 5
- Just D. W., et al., 2019, *ApJ*, **885**, 6
- Kennicutt Robert C. J., Keel W. C., van der Hulst J. M., Hummel E., Roettiger K. A., 1987, *AJ*, **93**, 1011
- Kilborn V. A., Koribalski B. S., Forbes D. A., Barnes D. G., Musgrave R. C., 2005, *MNRAS*, **356**, 77
- Kilborn V. A., Forbes D. A., Barnes D. G., Koribalski B. S., Brough S., Kern K., 2009, *MNRAS*, **400**, 1962
- Kleiner D., et al., 2019, *MNRAS*, **488**, 5352
- Koribalski B. S., et al., 2004, *AJ*, **128**, 16
- Koribalski B. S., et al., 2020, *Ap&SS*, **365**, 118
- Kormendy J., Kennicutt Robert C. J., 2004, *ARA&A*, **42**, 603
- Krumholz M. R., Burkhardt B., Forbes J. C., Crocker R. M., 2018, *MNRAS*, **477**, 2716
- Kurapati S., Chengalur J. N., Pustilnik S., Kamphuis P., 2018, *MNRAS*, **479**, 228
- Lagos C. d. P., Theuns T., Stevens A. R. H., Cortese L., Padilla N. D., Davis T. A., Contreras S., Croton D., 2017, *MNRAS*, **464**, 3850
- Lagos C. d. P., et al., 2018, *MNRAS*, **473**, 4956
- Larson R. B., Tinsley B. M., Caldwell C. N., 1980, *ApJ*, **237**, 692
- Lauberts A., Valentijn E. A., 1989, *The surface photometry catalogue of the ESO-Uppsala galaxies*
- Lee-Waddell K., et al., 2019, *MNRAS*, **487**, 5248
- Leroy A. K., Walter F., Brinks E., Bigiel F., de Blok W. J. G., Madore B., Thornley M. D., 2008, *AJ*, **136**, 2782
- Li J., Obreschkow D., Lagos C., Cortese L., Welker C., Džudžar R., 2020, arXiv e-prints, p. arXiv:2002.09083
- Lutz K. A., et al., 2017, *MNRAS*, **467**, 1083
- Maddox N., Hess K. M., Obreschkow D., Jarvis M. J., Blyth S.-L., 2015, *MNRAS*, **447**, 1610
- Maller A. H., Dekel A., 2002, *MNRAS*, **335**, 487
- Mancera Piña P. E., Posti L., Pezzulli G., Fraternali F., Fall S. M., Oosterloo T., Adams E. A. K., 2021a, arXiv e-prints, p. arXiv:2107.02809
- Mancera Piña P. E., Posti L., Fraternali F., Adams E. A. K., Oosterloo T., 2021b, *A&A*, **647**, A76
- Marasco A., Crain R. A., Schaye J., Bahé Y. M., van der Hulst T., Theuns T., Bower R. G., 2016, *MNRAS*, **461**, 2630
- Marcolini A., Brighenti F., D’Ercole A., 2003, *MNRAS*, **345**, 1329
- Martin D. C., et al., 2005, *ApJL*, **619**, L1
- Martinez-Delgado D., et al., 2010, *AJ*, **140**, 962
- Mayer L., Mastroiello C., Wadsley J., Stadel J., Moore B., 2006, *MNRAS*, **369**, 1021

- Merritt D., 1983, *ApJ*, 264, 24
- Mogotsi K. M., de Blok W. J. G., Caldú-Primo A., Walter F., Ianjamasimanana R., Leroy A. K., 2016, *AJ*, 151, 15
- Moore B., Katz N., Lake G., Dressler A., Oemler A., 1996, *Nature*, 379, 613
- Moorman C. M., Moreno J., White A., Vogeley M. S., Hoyle F., Giovanelli R., Haynes M. P., 2016, *ApJ*, 831, 118
- Murugesan C., Kilborn V., Obreschkow D., Glazebrook K., Lutz K., Džudžar R., Dénes H., 2019, *MNRAS*, 483, 2398
- Murugesan C., Kilborn V., Jarrett T., Wong O. I., Obreschkow D., Glazebrook K., Cluver M. E., Fluke C. J., 2020, *MNRAS*, 496, 2516
- Nikolic B., Cullen H., Alexander P., 2004, *MNRAS*, 355, 874
- Obreschkow D., Glazebrook K., 2014, *ApJ*, 784, 26
- Obreschkow D., Glazebrook K., Kilborn V., Lutz K., 2016, *ApJL*, 824, L26
- Omar A., Dwarakanath K. S., 2005a, *Journal of Astrophysics and Astronomy*, 26, 1
- Omar A., Dwarakanath K. S., 2005b, *Journal of Astrophysics and Astronomy*, 26, 71
- Osmond J. P. F., Ponman T. J., 2004, *MNRAS*, 350, 1511
- Parkash V., Brown M. J. I., Jarrett T. H., Bonne N. J., 2018, *ApJ*, 864, 40
- Posti L., Fraternali F., Di Teodoro E. M., Pezzulli G., 2018, *A&A*, 612, L6
- Putman M. E., et al., 1998, *Nature*, 394, 752
- Rasmussen J., Ponman T. J., Verdes-Montenegro L., Yun M. S., Borthakur S., 2008, *MNRAS*, 388, 1245
- Raymond J. C., Smith B. W., 1977, *ApJSS*, 35, 419
- Reynolds T. N., et al., 2019, *MNRAS*, 482, 3591
- Roberts I. D., Parker L. C., 2017, *MNRAS*, 467, 3268
- Robotham A. S. G., Obreschkow D., 2015, *Publ. Astron. Soc. Australia*, 32, e033
- Rogstad D. H., Lockhart I. A., Wright M. C. H., 1974, *ApJ*, 193, 309
- Romanowsky A. J., Fall S. M., 2012, *ApJSS*, 203, 17
- Rots A. H., Bosma A., van der Hulst J. M., Athanassoula E., Crane P. C., 1990, *AJ*, 100, 387
- Saintonge A., et al., 2017, *ApJSS*, 233, 22
- Schaye J., et al., 2015, *MNRAS*, 446, 521
- Schimminovich D., et al., 2010, *MNRAS*, 408, 919
- Sengupta C., Balasubramanyam R., 2006, *MNRAS*, 369, 360
- Serra P., et al., 2015, *MNRAS*, 448, 1922
- Skrutskie M. F., et al., 2006, *AJ*, 131, 1163
- Solanes J. M., Giovanelli R., Haynes M. P., 1996, *ApJ*, 461, 609
- Solanes J. M., Manrique A., Garcia-Gomez C., Gonzalez-Casado G., Giovanelli R., Haynes M. P., 2001, *ApJ*, 548, 97
- Stevens A. R. H., Brown T., 2017, *MNRAS*, 471, 447
- Stevens A. R. H., Lagos C. d. P., Obreschkow D., Sinha M., 2018, *MNRAS*, 481, 5543
- Stevens A. R. H., et al., 2019, *MNRAS*, 483, 5334
- Swaters R. A., van Albada T. S., van der Hulst J. M., Sancisi R., 2002, *A&A*, 390, 829
- Sweet S. M., Fisher D., Glazebrook K., Obreschkow D., Lagos C., Wang L., 2018, *ApJ*, 860, 37
- Tamburro D., Rix H. W., Leroy A. K., Mac Low M. M., Walter F., Kennicutt R. C., Brinks E., de Blok W. J. G., 2009, *AJ*, 137, 4424
- Toomre A., 1964, *ApJ*, 139, 1217
- Trinchieri G., Fabbiano G., Canizares C. R., 1986, *ApJ*, 310, 637
- Trinchieri G., Pellegrini S., Wolter A., Fabbiano G., Fiore F., 2000, *A&A*, 364, 53
- Tully R. B., 2015, *AJ*, 149, 171
- Verheijen M. A. W., Sancisi R., 2001, *A&A*, 370, 765
- Vollmer B., Cayatte V., Balkowski C., Duschl W. J., 2001, *ApJ*, 561, 708
- Vulcani B., Poggianti B. M., Finn R. A., Rudnick G., Desai V., Bamford S., 2010, *ApJL*, 710, L1
- Walter F., Brinks E., de Blok W. J. G., Bigiel F., Kennicutt Jr. R. C., Thornley M. D., Leroy A., 2008, *AJ*, 136, 2563
- Wang J., et al., 2017, *MNRAS*, 472, 3029
- Wang L., et al., 2018, *ApJ*, 868, 93
- Wen X.-Q., Wu H., Zhu Y.-N., Lam M. I., Wu C.-J., Wicker J., Zhao Y.-H., 2013, *MNRAS*, 433, 2946
- Westmeier T., Braun R., Koribalski B. S., 2011, *MNRAS*, 410, 2217
- Whiting M. T., 2020, in Ballester P., Ibsen J., Solar M., Shorridge K., eds, *Astronomical Society of the Pacific Conference Series Vol. 522, Astronomical Data Analysis Software and Systems XXVII*, p. 469
- Willmer C. N. A., Focardi P., da Costa L. N., Pellegrini P. S., 1989, *AJ*, 98, 1531
- Wong O. I., Meurer G. R., Zheng Z., Heckman T. M., Thilker D. A., Zwaan M. A., 2016, *MNRAS*, 460, 1106
- Wong O. I., et al., 2021, *MNRAS*
- Wright E. L., et al., 2010, *AJ*, 140, 1868
- Zasov A. V., Rubtsova T. V., 1989, *Soviet Astronomy Letters*, 15, 51
- Zhou Z., Wu H., Zhou X., Ma J., 2018, *PASP*, 130, 094101
- Zoldan A., De Lucia G., Xie L., Fontanot F., Hirschmann M., 2018, *MNRAS*, 481, 1376
- da Costa L. N., et al., 1988, *ApJ*, 327, 544
- van der Velden E., 2020, *The Journal of Open Source Software*, 5, 2004

APPENDIX A: TILTED-RING MODEL PARAMETERS AND PV DIAGRAM

In order to show the robustness of the model fitting to the galaxies, we take specific examples of two galaxies – NGC 1422 and ESO482-G027 (see Fig. 5) – for which the fitted model parameters such as their rotation curves (v_{rot}), inclination (i) and position angles (PA) are shown in Fig. A1. In addition, we also show the position-velocity (PV) diagram along the major and minor axis for the two galaxies. Overall, we find a good agreement between the fitted models and the data for the two galaxies.

APPENDIX B: COMPUTING THE RATIO OF SPECIFIC AM OF THE H I GAS AND STARS

We compute the total specific angular momentum of the H I gas and the stellar specific angular momentum following a method similar to computing j_b (see section 2.4), and as follows,

$$j_{\text{H I}} = \frac{\sum_i M_{\text{H I},i} v_{\text{rot},i} r_i}{\sum_i M_{\text{H I},i}}, \quad (\text{B1})$$

$$j_{\star} = \frac{\sum_i M_{\star,i} v_{\text{rot},i} r_i}{\sum_i M_{\star,i}}, \quad (\text{B2})$$

where $M_{\text{H I},i}$, $M_{\star,i}$, $v_{\text{rot},i}$ and r_i are the H I mass, stellar mass, rotation velocity and radius corresponding to the i^{th} ring, respectively. Following this we compute the ratio $j_{\text{H I}/j_{\star}}$ for the Eridanus sample. Fig. B1 shows the $j_{\text{H I}/j_{\star}}$ values plotted against the total baryonic mass (M_b) of the galaxies.

APPENDIX C: COMPARING THE VARIOUS H I DEFICIENCY PARAMETERS

Here we compare the Δf_q values for the Eridanus galaxies with other widely used H I deficiency parameters in the literature. We first compare the Δf_q values with the H I deficiency parameter (Δf_M), computed from the $f_{\text{atm}} - M_b$ scaling relation (see Fig. 3 in O16), using Eq. 7 in Li et al. (2020). This is shown in Fig. C1, and we find a good one-to-one agreement between the two H I deficiency parameters. In addition, we also compare the Δf_q values with more traditional H I deficiency parameters that are based on empirical scaling relations, such as the morphology dependent H I deficiency parameter first introduced by Haynes & Giovanelli (1984) (see Fig. C2), the morphology independent H I deficiency parameter calibrated for cluster-like galaxies by Chung et al. (2009),

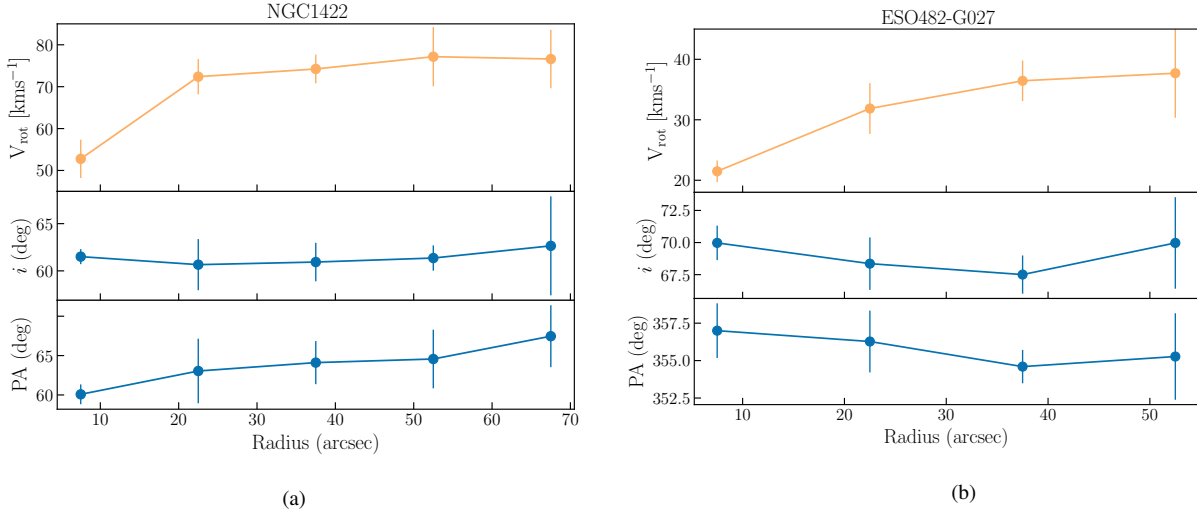


Figure A1. (a) The rotation curve, radially varying inclination (i) and position angle (PA) from the 3D model fitting using 3DBarolo for the NGC 1422 galaxy (b) Similar plot for the ESO482-G027 galaxy.

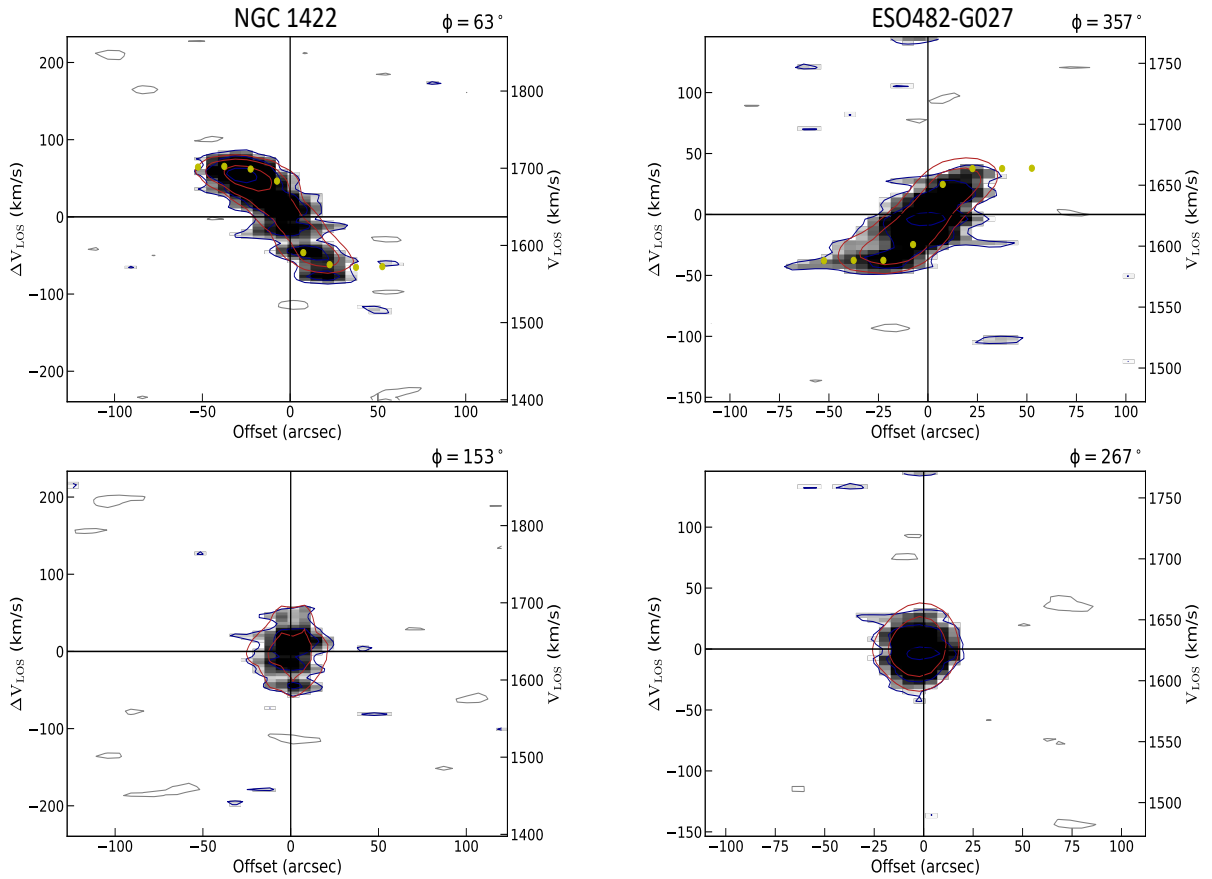


Figure A2. *Left:* Top panel shows the position-velocity (PV) diagram along the major axis of NGC 1422 produced by 3DBarolo after completing the fitting routine. The blue contours represent the data, and the red contours correspond to the final tilted-ring model, respectively. The yellow points correspond to the line-of-sight velocities $v_{\text{LOS}} = v_{\text{rot}} \sin(i)$ derived from the fit. Bottom panel shows the PV diagram along the minor axis of NGC 1422. *Right:* PV diagrams along the major (top panel) and minor axis (bottom panel) of ESO482-G027, respectively. The contours and points are as defined before. We find that for both galaxies the model and the derived v_{LOS} values are in good agreement with the observed data.

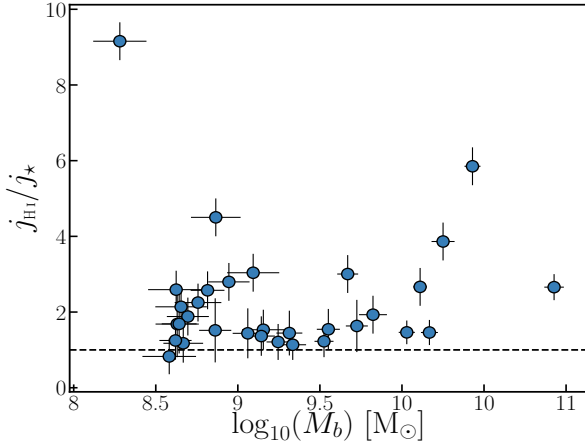


Figure B1. $j_{\text{H I}}/j_{\star}$ ratio plotted against the total baryonic mass, M_b . We see no correlation between the two parameters and find a mean value of $j_{\text{H I}}/j_{\star} \sim 2$. The black dashed line represents $j_{\text{H I}}/j_{\star} = 1$.

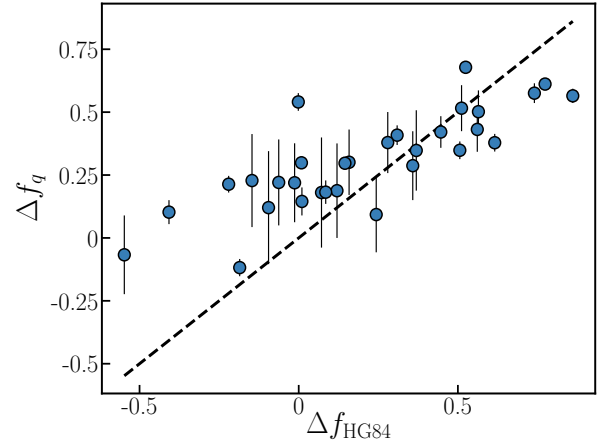


Figure C2. The Δf_q values plotted against the H I deficiency parameter introduced by Haynes & Giovanelli (1984).

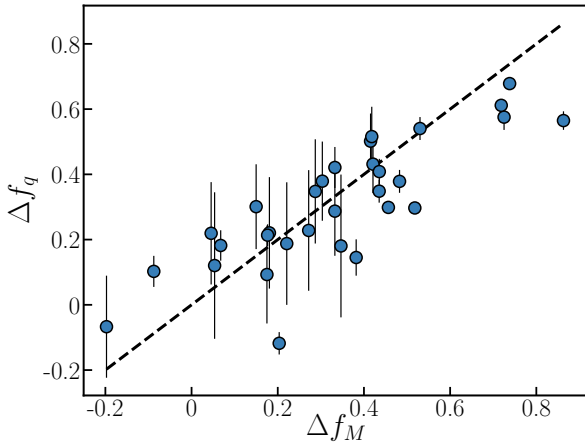


Figure C1. The Δf_q values plotted against the H I deficiency parameter Δf_M (see O16).

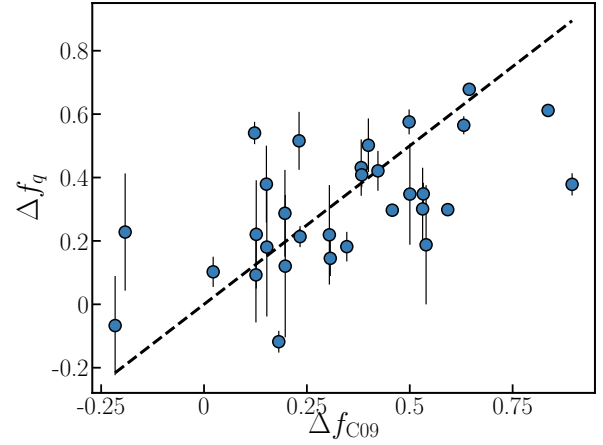


Figure C3. The Δf_q values plotted against the H I deficiency parameter as defined in Chung et al. (2009).

as shown in Fig. C3 and finally with the recently calibrated H I deficiency parameter derived by Dénes et al. (2014), based on the B-band photometric diameter of galaxies (see Fig. C4). We see that the Δf_q H I deficiency parameter overall shows a good one-to-one agreement with all the above H I deficiency parameters. This indicates the robustness of this physically motivated H I deficiency parameter, which is simply based on the deviation of the H I gas fraction of galaxies from the theoretical H I saturation, predicted by the analytical model in O16.

APPENDIX D: TABLE – PROPERTIES OF THE SAMPLE GALAXIES

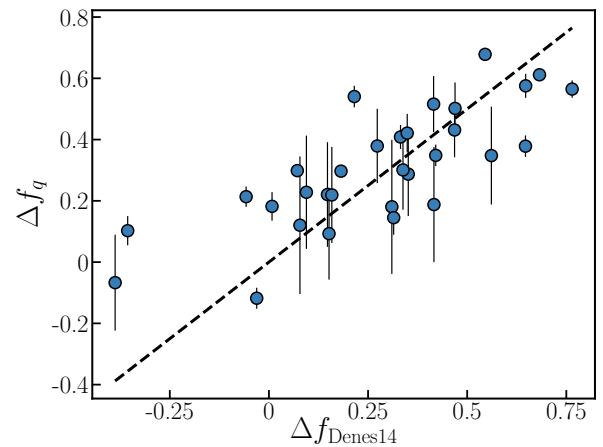


Figure C4. The Δf_q values plotted against the H I deficiency parameter defined by Dénes et al. (2014).

Table D1. The sample properties. Cols (1) - (2): WALLABY designation and common name; Cols (3) - (4): RA and DEC corresponding to the optical center; Col (5): Systemic velocity; Col (6): Luminosity distance; Col (7): Median value of position angle; Col (8): Median value of the inclination angle; Cols (9),(10),(11): H_I, stellar and total baryonic mass respectively; Col (12): total baryonic mass respectively; Col (13): atomic gas fraction; Col (14): disc stability parameter; Col (15): stability model based H_I deficiency parameter

WALLABY Name	Name	RA (J2000)	Dec (J2000)	V _{sys} (km s ⁻¹)	D (Mpc)	PA (°)	i (°)	log ₁₀ (M _{H I}) (M _⊙)	log ₁₀ (M _*) (M _⊙)	log ₁₀ (M _b) (M _⊙)	f _b (kpc km s ⁻¹)	f _{min}	q	Δf _q	
(1)	(2)	(3)	(4)	(5)	(6)	(7)	(8)	(9)	(10)	(11)	(12)	(13)	(14)	(15)	
Eridanus supergroup															
WALLABY032425-213233	NGC1325	03h24m25.57s	-21d32m38.5s	1588	20	232	72	9.32 ± 0.2	9.99 ± 0.05	10.1 ± 0.06	786 ± 56	0.22 ± 0.05	0.14 ± 0.05	0.18	
WALLABY032455-214701	ESO548-G011	03h24m55.30s	-21d47m02.0s	1456	18	142	57	7.98 ± 0.25	7.74 ± 0.15	8.27 ± 0.18	52 ± 16	0.7 ± 0.22	0.66 ± 0.31	0.18	
WALLABY032735-211339	ESO548-G021	03h27m35.29s	-21d13m42.2s	1686	21	72	67	8.51 ± 0.22	8.6 ± 0.09	8.92 ± 0.12	167 ± 38	0.52 ± 0.13	0.47 ± 0.19	0.3	
WALLABY032831-222957	ESO481-G028	03h28m32.22s	-22d43m04.8s	1774	23	338	53	8.17 ± 0.24	8.3 ± 0.11	8.6 ± 0.13	61 ± 15	0.5 ± 0.14	0.35 ± 0.15	0.29	
WALLABY032937-232103	ESO481-G030	03h29m38.31s	-23d42m01.2s	1657	21	230	63	8.29 ± 0.23	8.1 ± 0.11	8.59 ± 0.16	124 ± 34	0.68 ± 0.19	0.74 ± 0.32	0.19	
WALLABY032941-221642	NGC1347	03h29m41.50s	-22d17m06.0s	1755	22	315	34	8.49 ± 0.22	9.13 ± 0.07	9.24 ± 0.08	100 ± 14	0.24 ± 0.06	0.13 ± 0.05	0.15	
WALLABY033047-210333	ESO548-G029	03h30m47.17s	-21d03m29.6s	1292	16	95	53	7.7 ± 0.27	8.8 ± 0.11	8.84 ± 0.11	47 ± 9	0.1 ± 0.03	0.16 ± 0.06	0.56	
WALLABY033257-210513	ESO548-G034	03h32m57.63s	-21d05m21.9s	1665	21	81	29	8.07 ± 0.26	8.99 ± 0.1	9.06 ± 0.1	87 ± 13	0.14 ± 0.04	0.18 ± 0.06	0.58	
WALLABY033302-240756	ESO482-G005	03h33m02.25s	-24d07m38.3s	1915	25	261	79	8.95 ± 0.21	8.37 ± 0.07	9.15 ± 0.17	398 ± 104	0.84 ± 0.22	0.65 ± 0.28	0.12	
WALLABY033326-234246	IC1952	03h33m26.67s	-23d42m46.0s	1810	23	322	74	8.8 ± 0.21	9.65 ± 0.07	9.72 ± 0.07	277 ± 30	0.16 ± 0.04	0.12 ± 0.04	0.35	
WALLABY033341-212844	IC1953	03h33m41.87s	-21d42m43.1s	1859	24	129	44	9.07 ± 0.2	9.93 ± 0.06	10.01 ± 0.06	584 ± 44	0.16 ± 0.03	0.13 ± 0.04	0.21	
WALLABY033347-192946	NGC1359	03h33m47.71s	-19d29m31.4s	1964	25	322	58	9.56 ± 0.2	9.42 ± 0.06	9.88 ± 0.13	647 ± 96	0.65 ± 0.16	0.2 ± 0.07	-0.07	
WALLABY033501-245556	NGC1367	03h35m01.34s	-24d55m39.6s	1518	18	136	47	9.64 ± 0.2	10.3 ± 0.06	10.41 ± 0.07	1512 ± 92	0.23 ± 0.05	0.14 ± 0.04	0.1	
WALLABY033527-211302	ESO548-G049	03h35m28.07s	-21d13m01.3s	1518	19	115	64	8.22 ± 0.23	8.39 ± 0.08	8.67 ± 0.12	99 ± 21	0.48 ± 0.12	0.49 ± 0.19	0.38	
WALLABY033537-211742	IC1962	03h35m37.49s	-21d17m38.6s	1802	23	358	74	8.86 ± 0.21	8.74 ± 0.07	9.18 ± 0.13	255 ± 55	0.64 ± 0.16	0.39 ± 0.15	0.22	
WALLABY033617-253615	ESO482-G011	03h36m17.39s	-25d36m17.0s	1590	20	68	69	8.19 ± 0.26	8.66 ± 0.1	8.82 ± 0.11	89 ± 17	0.32 ± 0.09	0.31 ± 0.12	0.43	
WALLABY033653-245445	ESO482-G013	03h36m53.87s	-24d54m45.7s	1842	24	61	61	8.5 ± 0.22	8.51 ± 0.14	8.88 ± 0.14	92 ± 26	0.57 ± 0.15	0.29 ± 0.12	0.09	
WALLABY033728-243010	NGC1385	03h37m28.85s	-24d30m01.1s	1497	19	181	50	9.24 ± 0.2	10.08 ± 0.06	10.16 ± 0.06	341 ± 27	0.16 ± 0.03	0.05 ± 0.02	-0.12	
WALLABY033854-262024	NGC1398	03h38m52.13s	-26d20m16.2s	1373	17	278	44	9.32 ± 0.2	10.89 ± 0.07	10.9 ± 0.06	1488 ± 103	0.04 ± 0.01	0.04 ± 0.01	0.3	
WALLABY033921-212450	LEDA13460	03h39m21.43s	-21d24m56.6s	1622	21	240	45	8 ± 0.29	8.55 ± 0.14	8.69 ± 0.13	69 ± 15	0.28 ± 0.09	0.33 ± 0.13	0.49	
WALLABY033941-235054	ESO482-G027	03h39m41.21s	-23d50m39.8s	1622	21	356	69	8.28 ± 0.22	8.07 ± 0.1	8.58 ± 0.15	98 ± 15	0.69 ± 0.18	0.61 ± 0.2	0.23	
WALLABY034002-192200	ESO548-G065	03h40m02.70s	-19d21m59.8s	1216	15	38	66	8.01 ± 0.23	8.42 ± 0.08	8.6 ± 0.09	97 ± 15	0.35 ± 0.08	0.56 ± 0.2	0.5	
WALLABY034040-221711	ESO548-G070	03h40m40.99s	-22d17m13.4s	1774	23	64	67	8.35 ± 0.24	8.35 ± 0.12	8.72 ± 0.14	277 ± 64	0.58 ± 0.16	1 ± 0.43	0.35	
WALLABY034056-223350	NGC1415	03h40m56.86s	-22d33m52.1s	1552	20	334	66	8.87 ± 0.21	10.2 ± 0.08	10.23 ± 0.07	465 ± 41	0.06 ± 0.01	0.06 ± 0.02	0.3	
WALLABY034057-214245	NGC1414	03h40m57.04s	-21d42m47.3s	1695	22	354	65	8.42 ± 0.22	9 ± 0.08	9.13 ± 0.08	171 ± 22	0.26 ± 0.06	0.3 ± 0.1	0.42	
WALLABY034114-235017	ESO482-G035	03h41m14.83s	-23d45m13.0s	1885	24	180	47	8.64 ± 0.22	9.47 ± 0.08	9.55 ± 0.08	242 ± 27	0.17 ± 0.04	0.16 ± 0.05	0.41	
WALLABY034131-214051	NGC1422	03h41m31.07s	-21d40m53.5s	1644	21	64	61	8.32 ± 0.23	9.22 ± 0.09	9.29 ± 0.08	144 ± 17	0.14 ± 0.04	0.17 ± 0.06	0.38	
WALLABY034219-224520	ESO482-G036	03h42m18.80s	-22d45m09.2s	1569	20	193	50	8.35 ± 0.23	9.25 ± 0.09	9.32 ± 0.09	186 ± 26	0.14 ± 0.04	0.21 ± 0.07	0.54	
WALLABY034337-211418	ESO549-G006	03h43m38.17s	-21d14m15.7s	1612	21	209	66	8.44 ± 0.22	8.29 ± 0.09	8.75 ± 0.15	150 ± 37	0.65 ± 0.17	0.61 ± 0.25	0.22	
WALLABY034456-234158	LEDA13743	03h44m56.61s	-23d41m58.9s	1819	24	213	45	8.03 ± 0.28	8.43 ± 0.13	8.62 ± 0.13	46 ± 10	0.35 ± 0.11	0.26 ± 0.1	0.23	
WALLABY034517-230001	NGC1438	03h45m17.23s	-23d00m08.9s	1546	20	225	57	8.34 ± 0.23	9.62 ± 0.07	9.65 ± 0.07	264 ± 26	0.07 ± 0.02	0.14 ± 0.04	0.68	
WALLABY034814-212824	ESO549-G018	03h48m14.08s	-21d28m28.1s	1586	20	211	54	8.25 ± 0.24	9.47 ± 0.06	9.51 ± 0.06	192 ± 24	0.07 ± 0.02	0.14 ± 0.05	0.61	
Background galaxies															
WALLABY032434-215824	ESO548-G008	03h24m34.33s	-21d58m18.8s	4376	59	136	60	8.78 ± 0.38	8.57 ± 0.15	9.1 ± 0.25	171 ± 76	0.65 ± 0.3	0.32 ± 0.19	0.03	
WALLABY033138-250029	ESO482-G002	03h31m38.38s	-25d00m29.2s	6483	89	254	59	9.71 ± 0.26	10.28 ± 0.09	10.43 ± 0.09	1150 ± 172	0.25 ± 0.07	0.1 ± 0.03	-0.13	
WALLABY033147-211309	LEDA831121	03h31m48.07s	-21d13m08.2s	4244	57	56	43	8.81 ± 0.33	8.69 ± 0.15	9.16 ± 0.2	209 ± 73	0.6 ± 0.23	0.34 ± 0.17	0.09	
WALLABY033351-210315	LEDA13198	03h33m51.02s	-21d03m14.8s	6728	92	61	49	9.68 ± 0.29	10.13 ± 0.1	10.32 ± 0.11	689 ± 117	0.31 ± 0.09	0.08 ± 0.03	-0.34	
WALLABY033351-212725	WALLABY033351-212725	03h33m51.32s	-21d42m19.7s	4064	55	309	59	9.46 ± 0.16	9.74 ± 0.07	10 ± 0.07	820 ± 105	0.39 ± 0.07	0.19 ± 0.06	0	
WALLABY033757-213938	ESO548-G056	03h37m57.77s	-21d39m42.7s	4150	56	137	61	8.95 ± 0.32	9.41 ± 0.07	9.6 ± 0.11	405 ± 65	0.3 ± 0.1	0.24 ± 0.08	0.22	
WALLABY033810-194412	ESO548-G057	03h38m10.33s	-19d44m11.0s	4166	56	42	72	9.11 ± 0.33	8.79 ± 0.16	9.4 ± 0.23	380 ± 158	0.7 ± 0.28	0.35 ± 0.2	0.05	
WALLABY033859-223502	ESO482-G024	03h38m59.73s	-22d35m02.4s	4337	59	335	53	9.28 ± 0.22	8.91 ± 0.07	9.56 ± 0.17	554 ± 48	0.72 ± 0.22	0.36 ± 0.11	0.04	
WALLABY034421-204443	LEDA135108	03h44m21.72s	-20d44m43.2s	8008	111	269	63	9.62 ± 0.26	9.87 ± 0.07	10.14 ± 0.11	1254 ± 214	0.41 ± 0.12	0.21 ± 0.08	0.03	

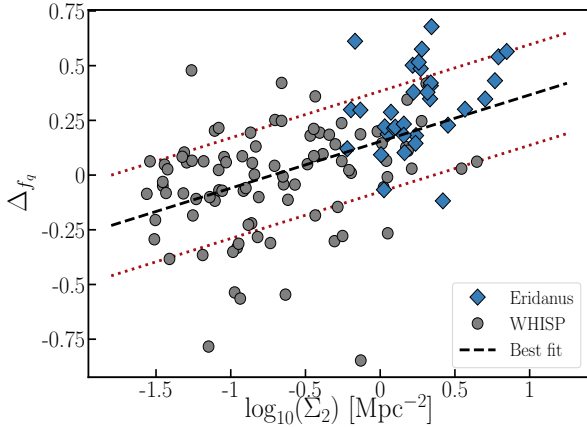


Figure E1. The Δf_q H I-deficiency parameter values for the Eridanus (blue diamonds) and the WHISP sample (grey circles) plotted against their $\log_{10}(\Sigma_2)$ local environment density estimates. The black dashed line is the best fit line to the data, and the red dotted lines represent the one sigma scatter about the distribution.

APPENDIX E: H I-DEFICIENCY PARAMETER VS Σ_2

As shown in Fig. 4 in section 3.3, galaxies in the Eridanus supergroup were not only observed to have higher Σ_2 values compared to galaxies in the WHISP sample, but it was also observed that those galaxies deviating the most from the $f_{\text{atm}} - q$ relation are from denser environments. Fig. E1 below highlights this trend, where the Δf_q values of both the Eridanus and WHISP galaxies are plotted against their local environment density (Σ_2). We find that there is a general trend of increasing H I-deficiency with increasing $\log_{10}(\Sigma_2)$ among both samples, clearly indicating that the H I gas in galaxies located in higher density environments have likely been affected by various environmental processes. We fit a linear regression of the form $\Delta f_q = \alpha \log_{10}(\Sigma_2) + b$ to the data and find a best fitting line with slope $\alpha = 0.21$ and a scatter of 0.23 dex. The few galaxies in the WHISP sample that lie below the lower 1σ scatter threshold are those galaxies that are currently interacting with their companions and accreting gas, therefore their H I gas fractions are boosted (implying Δf_q will be lower). These galaxies are discussed in more detail in M20.

This paper has been typeset from a $\text{\TeX}/\text{\LaTeX}$ file prepared by the author.